Global Biogeochemical Cycles

RESEARCH ARTICLE
10.1029/2019GB006520

Key Points:
- A biogeochemistry model was improved to quantify both GHG and energy fluxes between the biosphere and atmosphere
- Differences in radiative forcing among forest, hayfield, and cornfield were evaluated by considering both GHG and energy fluxes
- The differences in radiative forcing indicate slightly warming for changing forest to hayfield and warming for changing forest to cornfield

Supporting Information:
- Supporting Information S1

Correspondence to:
J. Deng and J. Xiao,
jia.deng@unh.edu;
j.xiao@unh.edu

Citation:
Deng, J., Xiao, J., Ouimette, A., Zhang, Y., Sanders-DeMott, R., Frolking, S., & Li, C. (2020). Improving a biogeochemical model to simulate surface energy, greenhouse gas fluxes, and radiative forcing for different land use types in northeastern United States. *Global Biogeochemical Cycles*, *34*, e2019GB006520. https://doi.org/10.1029/2019GB006520

Received 28 DEC 2019
Accepted 16 JUL 2020
Accepted article online 27 JUL 2020

Improving a Biogeochemical Model to Simulate Surface Energy, Greenhouse Gas Fluxes, and Radiative Forcing for Different Land Use Types in Northeastern United States

Jia Deng[1], Jingfeng Xiao[1], Andrew Ouimette[1], Yu Zhang[2], Rebecca Sanders-DeMott[1], Steve Frolking[1], and Changsheng Li[1]

[1]Earth Systems Research Center, Institute for the Study of Earth, Oceans and Space, University of New Hampshire, Durham, NH, USA, [2]Canada Centre for Mapping and Earth Observation, Natural Resources Canada, Ottawa, ON, Canada

Abstract Land use changes exert important impacts on climate, primarily through altering greenhouse gas (GHG) and surface energy fluxes. Biogeochemical models have incorporated a relatively complete suite of biogeochemical processes to simulate GHG fluxes. However, these models often lack detailed processes of surface energy exchange, limiting their ability to assess the impacts of land use change on climate. In this study, we incorporated processes of surface energy exchange into a widely used biogeochemistry model, DeNitrification-DeComposition (DNDC), so that it can quantify both GHG and energy fluxes between the biosphere and the atmosphere. When tested against field observations for the three dominant land use types (forest, hayfield, and cornfield) in the northeastern United States, the improved DNDC successfully captured the observed fluxes of outgoing shortwave radiation, latent heat, sensible heat, net ecosystem exchange of CO_2, and their differences among the three land use types. To evaluate the differences in radiative forcing among these land use types, we conducted 100-year simulations and converted the modeled GHG fluxes to radiative forcing using an atmospheric impulse response model. Our results show that the 100-year cumulative differences in net radiative forcing are 3.35 nW m^{-2} between the hayfield and forest (slight warming) and 43.2 nW m^{-2} between the cornfield and forest (warming) per hectare land use difference. The cooling effects of increased albedo after the conversion of forest to hayfield or cornfield (observed and modeled in recent years) are gradually offset by the warming effects of the increasing release of GHG as the forest becomes older.

1. Introduction

Human activities are primary drivers of land use change. For example, forest loss driven by shifting agriculture and commodity production accounted for about half of global forest loss between 2001 and 2015 (Curtis et al., 2018). Changes in land use and land cover are considered to have important impacts on climate, primarily through altering biophysical properties of the land surface (e.g., albedo, surface roughness, canopy conductance, and leaf area) and greenhouse gas (GHG) emissions (Dale, 1997; Feddema et al., 2005; Intergovernmental Panel on Climate Change, 2014). For example, forest conversion to crop fields can lead to both climate cooling through increased albedo and climate warming by emitting more GHG to the atmosphere (Betts, 2000; Bonan, 2008). Despite considerable research, large uncertainty remains over the magnitude and variability of climate forcing of land use change due to complex processes and interactions involved in land alterations (e.g., Bonan, 2008). In general, impacts of land use and land cover on climate can be divided into two major categories: biogeochemical and biogeophysical processes (Dale, 1997; Feddema et al., 2005; Sitch et al., 2005). Biogeochemical processes affect climate by changing the exchange rates of GHG and thereby the composition and radiative properties of the atmosphere. Biogeophysical processes directly affect biophysical parameters (e.g., albedo, surface roughness, canopy conductance, and leaf area) that determine the absorption and partitioning of energy at the Earth's surface. Quantifying the impacts of changes in land use and land cover on climate has been difficult because there are often tradeoffs between cooling and warming impacts due to land use changes, and these impacts can exhibit large spatial and temporal variability (e.g., Bonan, 2008; Kirschbaum et al., 2011).

Process-based modeling approaches have been developed to quantify the impacts of land use change on climate. These models have been applied from site to global scales to evaluate climate forcing due to land use change by assessing its impacts on different processes, such as energy and water balances, exchange of carbon dioxide (CO_2), and non-CO_2 GHG fluxes (e.g., Brovkin et al., 2006; Sitch et al., 2005). Biogeophysical-based models have been developed to simulate land surface processes of different land types. Although many improvements have been made through incorporating key atmosphere, biosphere, and biogeochemical processes, limitations and uncertainties still exist in biogeophysical-based models. For example, these models often lack detailed processes to explicitly simulate methane (CH_4) and nitrous oxide (N_2O) fluxes and have not incorporated management practices (e.g., harvest, tillage, fertilization, irrigation, and organic manure amendment) that regulate GHG fluxes (e.g., Bonan, 2008; Wu et al., 2016). Biogeochemical-based models, on the other hand, have incorporated relatively detailed biogeochemical processes to simulate GHG fluxes and impacts of environmental factors and human activities on GHG fluxes. However, biogeochemical models often lack processes to simulate biophysical properties and energy fluxes of different land use types.

The process-based biogeochemical model, DeNitrification-DeComposition (DNDC), has incorporated a relatively complete suite of biophysical and biogeochemical processes, which enables it to simulate vegetation growth, complex transport and transformations of carbon (C) and nitrogen (N), and GHG fluxes in terrestrial ecosystems (Li, 2000; Li et al., 1992a, 2012). Over the last three decades, DNDC has been widely used to simulate C and N cycling of different ecosystems and over various spatial and temporal scales (Gilhespy et al., 2014; Giltrap et al., 2010). However, the model has not incorporated detailed processes of surface energy exchange. This limitation in simulating energy exchange hinders applications of DNDC to assess the radiative forcing of different land types and the impacts of land use change on climate. To overcome this limitation and reduce uncertainties in assessing the radiative forcing of different land use/land cover types, we improved DNDC by incorporating processes simulating energy fluxes in the model. The improved DNDC model can explicitly simulate both GHG (CO_2, CH_4, and N_2O) and energy fluxes for different land cover types. We applied the model to assess radiative forcing of different land use types in the northeastern United States (i.e., the New England region). Although forest continuously increased following agricultural abandonment in the mid-1800s and is the primary land cover type in the northeastern United States, forest extent in this area declined by around 2.8% between 1990 and 2005 (Jeon et al., 2013) and has been projected to further decreasing driven by population growth, urbanization, and/or agriculture expansion (Thorn et al., 2017). The model was tested against field observations of energy and CO_2 fluxes from three different land use types (i.e., forest, hayfield, and cornfield (maize)) in the northeastern United States. We further applied the model to predict long-term (100-year) radiative forcing of the forest, hayfield, and cornfield by considering their differences in both albedo and GHG fluxes and analyzed the resulting differences in cumulative radiative forcing among these three dominant land use types in the northeastern United States. Because we did not simulate land use change and the associated changes in energy and GHG fluxes, the assessments of the climate impacts in this study do not represent the full climate impacts of the land use change.

2. Materials and Methods

2.1. The DNDC Model

DNDC is a process-based biogeochemical model developed for quantifying ecosystem C sequestration and the exchange of C and N gases between terrestrial ecosystems and the atmosphere (Li et al., 1992a, 1992b, 2000; Stange et al., 2000; Zhang et al., 2002). The model has been compared against measurements of GHG fluxes from various ecosystems in different countries (Gilhespy et al., 2014; Giltrap et al., 2010). DNDC is comprised of six interacting submodels: soil climate, plant growth, decomposition, nitrification, denitrification, and methanogenesis. The soil climate, plant growth, and decomposition submodels convert the primary drivers, such as climate, soil properties, vegetation, and anthropogenic activity (e.g., management), into soil environmental factors, such as soil temperature and moisture, pH, redox potential (Eh), and substrate concentrations. The nitrification, denitrification, and methanogenesis submodels simulate C and N transformations that are mediated by soil microbes and controlled by soil environmental factors (Li, 2000; Li et al., 2012).

In DNDC, net ecosystem exchange (NEE) of CO_2 is calculated as the difference between net primary production (NPP) and soil microbial heterotrophic respiration. NPP is simulated at a daily time step by considering the impacts of several environmental factors (e.g., solar radiation, air temperature, soil moisture, and N availability) on plant growth. The model simulates the production of plant biomass and litter and incorporates the litter into pools of soil organic matter (SOM). Soil heterotrophic respiration is calculated by simulating the decomposition of SOM. The model divides SOM into four pools: litter, microbes, humads, and passive humus. Each pool is further divided into two or three subpools with specific C:N ratios and decomposition rates. As a microbially mediated process, the decomposition of each SOM pool depends on its specific decomposition rate as well as soil thermal and moisture conditions (Li et al., 2012). In addition to CO_2 fluxes, DNDC has incorporated a relatively complete suite of biogeochemical processes to simulate CH_4 and N_2O fluxes from terrestrial ecosystems. Methane flux is predicted by modeling CH_4 production, oxidation, and transport processes (Deng et al., 2017). The model simulates soil N dynamics at an hourly or daily time step through tracking a series of biogeochemical reactions: decomposition, microbial assimilation, plant uptake, ammonia volatilization, ammonium adsorption, nitrification, denitrification, and nitrate leaching. Fluxes of N gases (i.e., NH_3, NO, N_2O, and N_2) are predicted as either products or intermediate products by simulating the relevant N transformation processes. Further details regarding the DNDC structure, inputs, and outputs, as well as the physical, chemical, and biogeochemical processes incorporated into the model's framework, are available in Gilhespy et al. (2014), Li (2000), and Li et al. (2000, 2012).

2.2. Modification of DNDC

To quantify the radiative forcing (W m^{-2}) of energy and GHG fluxes for different land use types, we improved the DNDC model by incorporating simple parameterizations of energy exchange between soil, vegetation, and the atmosphere. The improved model simulates vertical energy fluxes among the soil, vegetation, and atmosphere by assuming that these components are horizontally uniform (Figure 1a). New processes that have been incorporated into DNDC include reflection of shortwave radiation (SW), allocation of SW between the canopy and ground surface, longwave radiation emission and absorption (LW), latent heat flux (LH), sensible heat flux (SH), and conductive heat flux in the ground (Figure 1a).

2.2.1. Energy Balance of Canopy

The model simulates the plant canopy as a single layer. The predicted energy balance terms include SW, LW, SH, LH, and the change of heat contained in the whole vegetation canopy layer. The energy balance of the canopy is written as follows:

$$L_v + S_v = H_v + \lambda E_v + C_v{*}\mathrm{d}T_v/\mathrm{d}t$$

where L_v is the net longwave radiation absorbed by the canopy, S_v is the net shortwave radiation absorbed by the canopy, H_v is the sensible heat flux from the canopy, λE_v is the latent heat flux from the canopy (λ is the latent heat of vaporization and E is the evapotranspiration), C_v is the canopy heat capacity and is estimated on the basis of plant biomass and the specific heat capacity of moist biomass according to Moore and Fisch (1986), and T_v is canopy temperature.

The net LW absorbed by vegetation considers exchanges of LW between the canopy and both the ground surface and the overlying atmosphere (Equation A2 and Figure 1b). Upward LW from the ground (Equation A3) includes the reflected part of the downward LW below the vegetation (Equation A4) and the upward LW directly from the ground surface. Net SW is partitioned to the canopy and ground, with the net SW intercepted by the canopy estimated on the basis of albedo and leaf area index (LAI) (Equation A5 and Figure 1c). LAI is calculated as a function of total leaf carbon and specific leaf area (Song et al., 2013).

Sensible heat flux from the vegetation is directly related to canopy temperature and canopy air temperature (Equation A8), and the canopy air temperature is calculated based on air temperature, canopy temperature, temperature of the ground surface, and aerodynamic resistances from the canopy air to the atmosphere, the ground to canopy air, and leaf surface to canopy air (Equation A9) (Oleson et al., 2013). The aerodynamic resistances between the canopy and the atmosphere (r_{va}) and between the ground and the canopy (r_{gv}) are estimated on the basis of Choudhury and Monteith (1988) (Equations A11 to A13 for r_{va} and Equations A15 and A16 for r_{gv}). The zero plane displacement and the roughness lengths used for calculating r_{va} and r_{gv} are estimated on the basis of canopy height or set as fixed values for the ground surface (Campbell

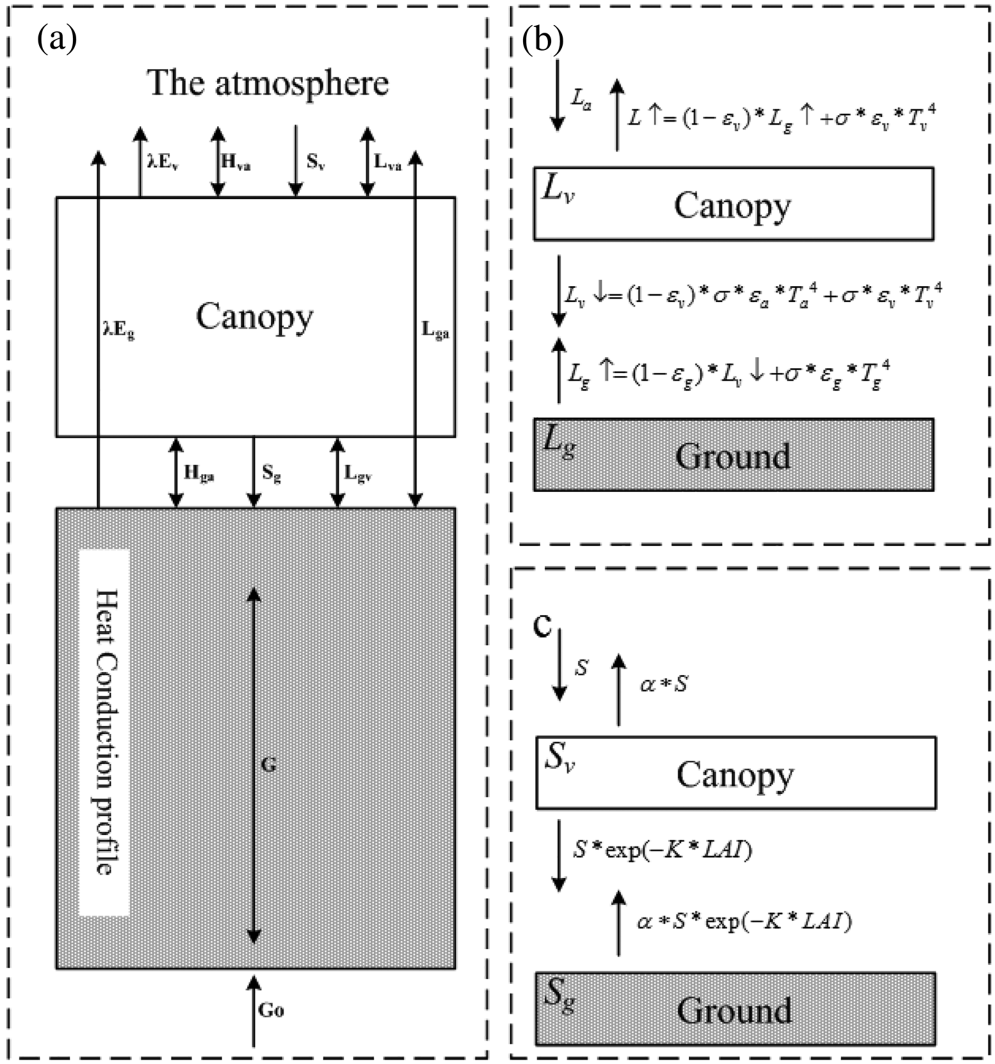

Figure 1. (a) The simulated energy fluxes between soil, vegetation, and the atmosphere, (b) schematic diagram of longwave radiation absorbed, transmitted, and reflected by canopy and ground, and (c) schematic diagram of solar radiation absorbed, transmitted, and reflected by canopy and ground. λE, H, S, L, G, and Go are the latent heat flux, sensible heat flux, solar radiation, longwave radiation, conductive heat flux, and geothermal flux, respectively. The subscripts, g, v, and a, indicate ground surface, vegetation canopy, and the atmosphere, respectively, and are used to identify energy fluxes between different components.

& Norman, 2012). The aerodynamic resistance between the leaf and canopy air (r_b) is estimated using canopy wind (Equation A14) and the turbulent transfer coefficient between the canopy surface and canopy air (Equation A14) (Oleson et al., 2013).

Latent heat from the canopy is estimated with the Penman-Monteith equation (Equation A10) (Monteith, 1965) using the available energy absorbed by the canopy and canopy resistance. Canopy resistance is simulated as in Liu et al. (1999), which considers the impacts of solar radiation, temperature, vapor pressure deficit, and leaf water potential on stomatal resistance. When canopy-intercepted water is available, latent heat flux consumes the intercepted water and canopy resistance is set to 0.

2.2.2. Energy Balance of Ground Surface

The energy balance of the ground surface is simulated as follows:

$$L_g + S_g = H_g + \lambda E_g + G_s$$

where L_g is the net LW absorbed by the ground surface, S_g is the net SW absorbed by the ground surface, H_g is the sensible heat flux from ground, λE_g is the latent heat flux from ground, and G_s is the ground heat flux.

The net LW absorbed by ground consists of absorbed downward LW below the vegetation and upward LW directly from the ground surface (Equation A18 and Figure 1b). The net SW on the ground is estimated on the basis of ground albedo and LAI (Equation A19 and Figure 1c). The ground albedo is a fixed value during the snow free period and is weighted based on snow and bare ground albedo according to snow cover fraction during the periods with snow cover (Equations A20 to A22). Snow albedo is calculated as a function of age of surface snow (Equation A21) that is determined by the number of days since the last snowfall (Hansen et al., 1983).

Sensible heat flux above the ground surface is calculated based on canopy air temperature, ground surface temperature, and the resistance between the ground and canopy air (Equation A24). Latent heat flux from the ground surface is also estimated by the Penman-Monteith method (Equation A25) (Monteith, 1965). The soil resistance (r_s) for calculating LH from the ground surface is estimated on the basis of soil moisture (Equation A26) (Sun, 2005). The soil resistance is set to 0 s m^{-1} if the surface is covered by snow.

The heat flux from the ground surface to the underlying layer is calculated using the temperature gradient between the surface and the snow (only when snow is present) or upper soil layer (at midpoint of the layer) (Equation A27). The improved DNDC calculates the temperature of the ground surface by iterative calculation of the surface energy balance. The heat flux to snow or soil profile is then calculated based on the temperature of the ground surface and the snow or the upper soil layer.

2.3. Study Area and Field Data

Our study focused on three different land use/cover types (i.e., forest, hayfield, and cropland) in a midlatitude temperate region of the northeastern United States. These three land use types represent dominant forest and deforested land use types in the study region (Burakowski et al., 2018). The field data used to support the model testing and application were collected at three sites located within 8 km of one another in New Hampshire. This area has a humid continental climate, with warm and humid summers and long, cold, and snowy winters. The sites are characterized by a mean annual air temperature of 8.9°C, average annual precipitation of 1,168 mm, and average total annual snowfall of 114 cm from 1981 to 2010 according to the observations from the local weather station (NOAA National Centers for Environmental Information, 2010).

The forest site is dominated by the broadleaf deciduous temperate forest composed primarily of red maple (*Acer rubrum*), northern red oak (*Quercus rubra*), white oak (*Quercus alba*), white pine (*Pinus strobus*), and shagbark hickory (*Carya ovata*). The hay and crop types were C3 nonarctic grass and corn during the measurement period from 2014 to 2016 (Table 1; Burakowski et al., 2018). The forest site was unmanaged, while intensive farming management practices (FMPs), such as planting and harvest, fertilization, manure amendment, and tillage, have been applied at both the hayfield and cornfield. The hayfield received inputs of C (around 380 g C m^{-2} $year^{-1}$) and N (around 28.3 g N m^{-2} $year^{-1}$) as organic manure from 2014 to 2016. The hay was harvested two or three times in each year. At the cornfield, corn was planted in May and harvested in October, and the field received inputs of C (around 380 g C m^{-2} $year^{-1}$) and N (around 38.1 g N m^{-2} $year^{-1}$) as organic manure and/or synthetic fertilizers from 2014 to 2016. The organic manure was applied in each year from 2014 to 2016, while the synthetic fertilizers were applied in 2015 and 2016. The FMPs represent typical management applied in the local area. Table 1 summarizes the general characteristics, soil texture, and the FMPs of our study sites.

The field data used to test the improved DNDC model include outgoing shortwave radiation (OSW), LH, SH, and NEE. The energy and CO_2 fluxes were measured using three eddy covariance towers that sampled meteorological and near-surface eddy covariance fluxes at half-hourly intervals during the period from 2014 to 2016. Energy and CO_2 fluxes were sampled using a tower-mounted LI-COR® LI-7200 enclosed path CO_2/H_2O analyzer and Gill® Windmaster sonic anemometer at 3.6-m height at the hayfield, 5 m at the corn field, and 28 m at the forest site. OSW was measured using Kipp & Zonen CNR4 net radiometers (Burakowski et al., 2018). Turbulent fluxes were calculated using the EddyPro® (Version 6.2.1, LI-COR Biosciences) open source software. The nighttime NEE measurements made during low-turbulence conditions with potential advective losses of CO_2 were identified and removed when friction velocity was below a calculated site-specific threshold (Papale et al., 2006). Positive NEE values represent net CO_2 fluxes into the atmosphere, and negative fluxes represent net CO_2 uptake. The gap filling of the NEE fluxes was performed using the marginal distribution sampling methodology (Reichstein et al., 2005) implemented in

10.1029/2019GB006520

Table 1
General Characteristics and Soil Properties of the Studied Forest, Hayfield, and Cornfield

Land type	Latitude/longitude	Plant type	Soil texture	Management
Forest	43.11°N, 70.95°W	BDTF[a]	Myers clay	None
Hayfield	43.17°N, 70.93°W	C3 grass	Myers clay	Tillage, cutting, and dairy manure amendment
Cornfield	43.14°N, 70.96°W	Corn	Silty clay loam	Tillage, planting, harvest, fertilization, and dairy manure amendment

[a]BDTF, broadleaf deciduous temperate forest.

the R-based (R Core Team, 2016) eddy covariance processing tool, REddyProc (Wutzler et al., 2018). The daily energy and NEE fluxes were calculated as the average and cumulative values of the half-hourly measurements, respectively. The climate and soil properties of the three sites and the FMPs for the hayfield and cornfield were also recorded for the duration of the energy and NEE measurements. These field measurements provide an opportunity to evaluate the performance of the improved DNDC model for predicting both energy and CO_2 fluxes and to assess the radiative forcing of different land use types in the study region. The technical details regarding the measurements of energy fluxes and NEE, and the relevant auxiliary variables are described by Burakowski et al. (2018) and Sanders-DeMott et al. (2019).

2.4. Model Application

2.4.1. Model Evaluation

The improved DNDC was run for the forest, hayfield, and cornfield for the period from 2014 to 2016. Daily meteorological data (i.e., maximum, mean, and minimum air temperatures, precipitation, incoming SW, wind speed, and humidity) from 2014 to 2016 were obtained from either on-site measurements or the two United States Climate Reference Network (USCRN) stations colocated with the hay (Durham 2SSW) and forest (Durham 2N) sites (Bell et al., 2013; Diamond et al., 2013) to test the improved model. The primary soil input parameters, including soil texture, clay fraction, bulk density, pH, and soil organic carbon content, were determined using on-site records for the three sites (Tables 1 and 2). The input parameters of FMPs, including planting and harvest dates, tillage, fertilization, and application of organic manure, were derived from the field records (Table 2).

The incorporation of the energy exchange processes into DNDC introduced several new model parameters. These parameters were either set to the literature values or calibrated against energy flux measurements in 2014 (Table 2). The calibrated parameters related to energy fluxes included canopy and soil albedo values. The canopy albedo for forest, corn, and hay were calibrated within their variation ranges of 0.12 to 0.19 for forest, 0.16 to 0.22 for corn, and 0.17 to 0.25 for hay (Cox et al., 1999; Hollinger et al., 2010; Markvart & Castañer, 2003). The soil albedo was calibrated within its variation range of 0.10 to 0.20 (Wilson & Henderson-Sellers, 1985). In order to simulate plant growth, DNDC also requires phenological and physiological parameters, including annual maximum biomass production and its partitioning to shoot and root, vegetation C/N ratio, required thermal degree days for vegetation growth, plant water requirement, and an index of biological N fixation. These parameters for the three land use types were determined either based on the literature, as model defaults, or calibrated against the observations in 2014 (Table 2).

For each site, we ran the improved model for 2014 (calibration) and continuously from 2014 to 2016, with 2015 and 2016 for validation. The model was tested against the measured OSW, LH, SH, and NEE. Two statistical measures, the relative root-mean-square error (RRMSE, Equation 1) and the correlation coefficient (R, Equation 2), were used to quantify the accordance and correlation between model predictions and field observations (Moriasi et al., 2007).

$$\mathrm{RRMSE} = \frac{100}{|\overline{o}|}\sqrt{\frac{\sum_{i=1}^{n}(p_i - o_i)^2}{n}} \tag{1}$$

$$R = \frac{\sum_{i=1}^{n}(o_i - \overline{o})(p_i - \overline{p})}{\sqrt{\sum_{i=1}^{n}(o_i - \overline{o})^2 \sum_{i=1}^{n}(p_i - \overline{p})^2}} \tag{2}$$

In both equations, o_i and p_i are the observed and simulated values, respectively, $\overline{o}$ and $\overline{p}$ are their averages, and n is the number of values.

Table 2
Primary Model Parameters for the Forest, Hayfield, and Cornfield

Model parameters	Forest	Hay	Corn	Data source
Snow-free canopy albedo	0.12	0.25	0.20	Calibrated
Soil albedo	0.17	0.17	0.17	Calibrated
Canopy emissivity	0.98	0.98	0.98	Sobrino et al. (2005)
Soil emissivity	0.94	0.94	0.94	Sobrino et al. (2005)
Snow emissivity	0.98	0.98	0.98	Snyder et al. (1998)
Soil bulk density (g cm^{-3})	1.01	0.87	1.12	Field records
Clay content (%)	10	11	20	Field records
Soil organic matter content (%)	3.6	2.0	2.6	Field records
pH	4.4	6.3	6.8	Field records
Ground heat flux (W m^{-2})	0.57	0.57	0.57	Pollack and Chapman (1977)
MP[a] (g C m^{-2})	1,200	900	825	Calibrated
The shoot and root fractions	0.65/0.35	0.65/0.35	0.86/0.14	Calibrated; Bolinder et al. (2007)
C/N[b]	148	58	51	Calibrated
TDD[c] (°C · day)	3,500	3,700	2,300	Calibrated
WR[d] (g water g^{-1} dry matter)	150	300	150	Calibrated
NFI[e]	No fixation	No fixation	No fixation	Default
Specific leaf area (m^2 g C^{-1})	0.02	0.04	0.04	Calibrated; Song et al. (2013)
		C input from manure (g C m^{-2})		
2014	0	380	380	Field records
2015	0	380	380	Field records
2016	0	380	380	Field records
		N input from manure and fertilizers (g N m^{-2})		
2014	0	28.3	38.1	Field records
2015	0	28.3	38.1	Field records
2016	0	28.3	38.1	Field records

[a]MP, the annual maximum productivity under optimum growing conditions. [b]C/N, carbon to nitrogen ratio of the plant biomass. [c]TDD, the required accumulated air temperature heat sum above a 0 °C threshold during the growing season for full vegetation growth. [d]WR, amount of water required by the plant (g water g^{-1} dry matter). [e]NFI, index of biological nitrogen fixation.

2.4.2. Differences in Radiative Forcing Among Land Use Types

To investigate the long-term dynamics of radiative forcing for the typical forest and deforested land cover types in northeastern Unites States under current climate conditions, we conducted 100-year simulations to predict both energy and GHG fluxes for the forest, hayfield, and cornfield. DNDC was driven by recent climate data from 2001 to 2016 that were produced by the DAYMET model (Thornton et al., 2018). Specifically, we ran the model using the historical climate data from 2001 to 2016 and then ran for another 84 years using the climate data randomly selected from the 2001–2016 climate records. Therefore, the climate conditions in this long-term simulations are representative of "current" climate scenario. During the simulations, no FMPs were applied at the forest site, and the FMPs for the hayfield and cornfield were based on the field records that are representative of the local conditions. We set a full hay growth cycle as 5 years. The hay field was plowed and resown every 5 years and was additionally cut two or three times in each year depending growth. At the cornfield, corn was planted in May and harvested in October in each year. We collected the simulated OSW, net CO_2, CH_4, and N_2O fluxes (the sign convention for the GHG fluxes is that positive values represent net GHG fluxes into the atmosphere and negative fluxes represent net GHG uptake) of the three sites for analysis. The net CO_2 fluxes for the studied land use types (Equation 3) were calculated as follows:

$$\text{Net } CO_2 \text{ flux} = \text{NEE} - C_{input} + C_{harvest} \tag{3}$$

where C_{input} is the C input through manure application (0.0 for forest and 380 g C m^{-2} $year^{-1}$ for hay and corn) and root incorporation (only for hay in the years of termination) and $C_{harvest}$ is the carbon exported from the ecosystem through corn harvesting or hay cutting that is assumed be released to the atmosphere within the year of harvesting. We assume that there is no forest harvest or major disturbance (e.g., fire) during the 100-year simulation.

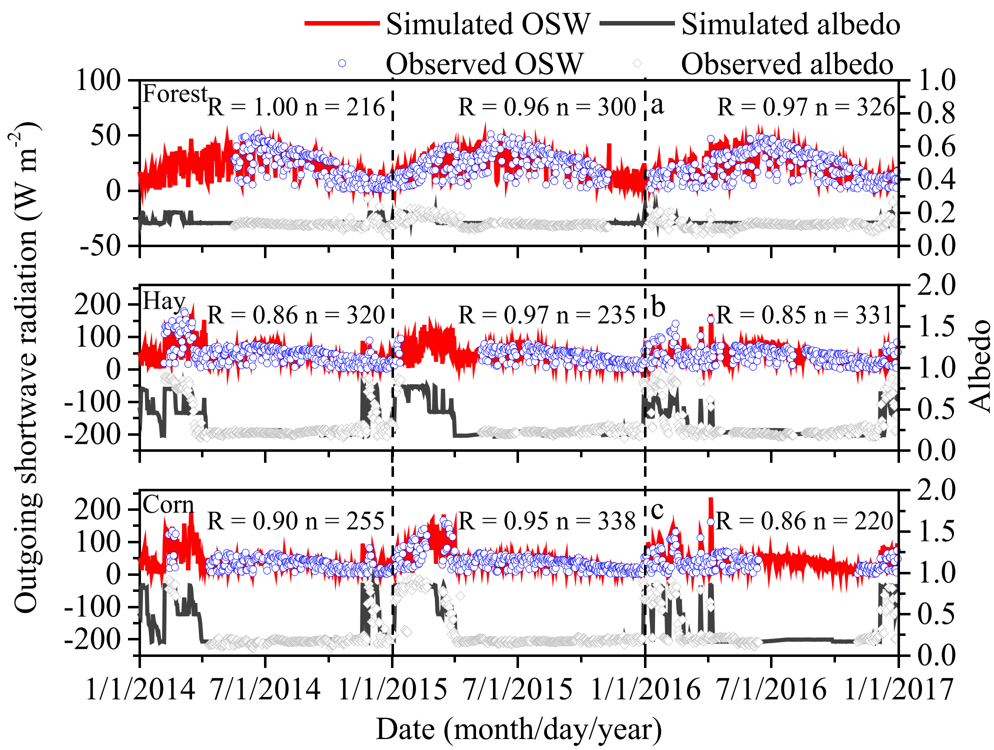

Figure 2. Simulated and observed daily outgoing shortwave radiation (OSW) and albedo at the (a) forest, (b) hayfield, and (c) cornfield during the period from 2014 to 2016. The statistical measures were for OSW, and the correlations between the simulated and observed daily OSW were significant for all cases ($P < 0.0001$). Note that the vertical axis scales for OSW and albedo are different across the three sites.

To evaluate the differences in radiative forcing among the studied land use types, we used a simple atmospheric impulse response model and assumed that net GHG fluxes are small perturbations to the global atmosphere (Frolking & Roulet, 2007; Frolking et al., 2006). We calculated radiative forcing induced by GHG fluxes using the site-specific DNDC simulated net CO_2, CH_4, and N_2O fluxes to drive the atmospheric impulse response model among the three land use types. The atmospheric impulse response approach can compare radiative forcing due to different GHG fluxes during variable time horizons and goes beyond calculations based on the global warming potential method (Intergovernmental Panel on Climate Change, 2014) by (1) allowing for a time series of gas flux input instead of only a single pulse input and (2) providing the instantaneous radiative forcing for each year of the simulation, instead of CO_2 equivalent. We also calculated the differences in radiative forcing due to the differences in albedo among the three land use types by assuming that different OSWs are small perturbations to the global atmosphere and the perturbations are spread evenly across the earth surface. Specifically, the differences in radiative forcing due to the differences in OSW were calculated by referring to Kirschbaum et al. (2011) (Equation 4):

$$\Delta R_S = -\Delta S\uparrow^*(1 - A_{\mathrm{atm}})/\mathrm{Area}_{\mathrm{earth}} \tag{4}$$

where $\Delta S\uparrow$ is the difference in OSW between the land use types, A_{atm} is the proportion of shortwave radiation absorbed by the atmosphere, and $\mathrm{Area}_{\mathrm{earth}}$ is the area of the Earth's surface (5.1×10^{14} m^2). We set the A_{atm} as 0.28 by referring to Zhao and Jackson (2014), who analyzed radiative forcing of land use changes in North America. Since the three sites are within 8 km of each other, it is not likely that there are significant intersite differences in atmospheric effects on radiative transfer.

By calculating radiative forcing (e.g., W m^{-2}), the SW and three greenhouse gases can be compared in common units at any time. Because we compared the radiative forcing difference between 1 ha of different land use types, we expressed the results as watt per square meter per hectare. Please note that we only focused on impacts on the global scale because we calculated the radiative forcing to the global atmosphere, and we did

Table 3
Comparison of the Modeled (M) and Observed (O) Outgoing Shortwave Radiation, Latent Heat Flux, Sensible Heat Flux (W m^{-2}), and Net Ecosystem Exchange of CO_2 (NEE; in g CO_2-C m^{-2}) During the Period From 2014 to 2016 at the Forest, Corn, and Hay Sites

	Forest			Hay			Corn		
Year	O[a]	M	RRMSE[b]	O	M	RRMSE	O	M	RRMSE
Outgoing shortwave radiation									
2014	NA[59]	22.1	NA	47.9[88]	46.5	2.8	37.7[70]	42.2	11.9
2015	22.0[82]	23.3	5.8	NA [64]	45.7	NA	41.5[93]	45.0	8.4
2016	21.1[89]	22.5	6.4	43.0[90]	42.4	1.5	NA[60]	41.2	NA
Latent heat flux									
2014	NA[45]	56.4	NA	51.9[91]	51.6	0.5	45.2[75]	45.6	1.0
2015	56.4[78]	57.1	1.2	NA[55]	47.8	NA	45.5[91]	40.4	11.3
2016	52.4[98]	49.3	5.9	45.8[92]	45.1	1.6	47.4[76]	42.8	9.7
Sensible heat flux									
2014	NA[45]	23.5	NA	6.0[90]	5.9	1.6	16.2[74]	13.5	16.3
2015	34.8[78]	27.9	20.0	NA[53]	12.5	NA	20.0[89]	19.2	3.9
2016	32.8[98]	31.9	3.2	9.4[91]	14.1	50.1	21.0[76]	19.0	9.5
Net ecosystem exchange of CO_2									
2014	NA[45]	−440.9	NA	−146.7[91]	−193.9	32.2	48.6[75]	52.1	7.2
2015	−547.3[78]	−495.8	9.4	NA[55]	−157.0	NA	39.5[91]	21.4	30.2
2016	−326.3[93]	−439.7	34.8	−119.8[92]	−149.1	24.5	−47.4[76]	−50.3	6.0

[a]Each number within the bracket is the percentage of the days when daily observations were available in each year. In order to calculate the annual total energy and CO_2 fluxes in each year, fluxes for the days lacking observations were gap-filled using the mean fluxes of the corresponding month that were calculated based daily fluxes from 2014 to 2016. Daily fluxes from either direct observations or gap filling were then summed up to calculate the annual total fluxes. The annual total fluxes were not calculated for those years when the data coverage was less than 70%. [b]RRMSE is relative root-mean-square error (%).

not consider impacts on climate of differences in the partitioning of available energy into LH and SH. While LH and SH fluxes can affect atmospheric humidity and cloudiness, our three sites are close to each other, so any site-level differences in these fluxes are not likely to cause persistent differences in site-level atmospheric modification of radiative forcing.

3. Results and Analyses

3.1. Model Evaluation

3.1.1. Outgoing Shortwave Radiation

Both the seasonal patterns and magnitudes of OSW varied across the three land use types (Figure 2). At the forest site, OSW was lower during the winter and higher during the summer, although albedo was slightly higher during the winter with snow cover. In contrast, both OSW and albedo were relatively high during the winter season with snow cover and relatively low in the summer season at both the hay and corn sites. The improved DNDC model captured the differences in the seasonal patterns of OSW and albedo across the three land use types for both the calibration (2014) and validation periods (2015 and 2016). The correlation coefficient (R) values between the modeled and observed OSW from 2014 to 2016 ranged from 0.96 to 1.00 for the forest, from 0.85 to 0.97 for the hayfield, and from 0.86 to 0.95 for the cornfield ($p < 0.0001$; Figure 2). The improved DNDC also captured the different magnitudes of OSW across the three land use types. The simulated annual OSW during the period from 2014 to 2016 ranged from 22.1 to 22.5 W m^{-2} for the forest, 42.4 to 46.5 W m^{-2} for the hayfield, and 41.2 to 45.0 W m^{-2} for the cornfield. The observations of the corresponding types ranged from 21.1 to 22.0, 43.0 to 47.9, and 37.7 to 41.5 W m^{-2}, respectively. The RRMSE between the simulated and observed annual OSW varied from 5.8% to 6.4% for the forest, 1.5% to 2.8% for the hayfield, and 8.4% to 11.9% for the cornfield (Table 3). Both the simulations and observations demonstrated that the annual OSW at the forest was lower than that at the hayfield and cornfield (Table 3). Please note that the RRMSE was not calculated for the comparisons when the observed annual total OSW was not available.

3.1.2. Latent Heat

The improved DNDC also generally captured the seasonal dynamics and magnitudes of LH above the canopy for the three land use types. Both the simulations and observations showed that the LH was relatively low during the nongrowing seasons and relatively high during the growing seasons, although some low values appeared in the growing seasons primarily due to low incoming SW, dry soils, or hay cutting

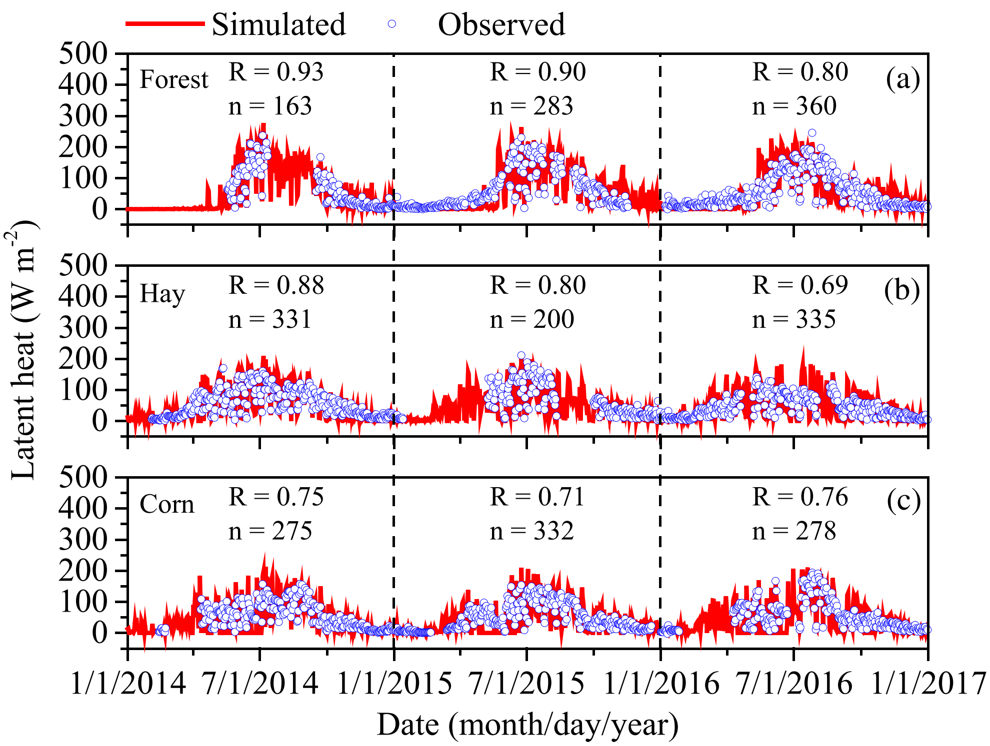

Figure 3. Simulated and observed daily latent heat fluxes at the forest (a), hayfield (b), and cornfield (c) during the period from 2014 to 2016. The correlations between the simulated and observed daily latent heat fluxes were significant for all cases ($P < 0.0001$).

(Figure 3). The R values between the simulations and field observations from 2014 to 2016 varied from 0.80 to 0.93, 0.69 to 0.88, and 0.71 to 0.76, for the forest, hayfield, and cornfield, respectively. The simulated seasonal variations of LH were significantly correlated with the observations for both the calibration and validation years ($p < 0.0001$). The simulated annual LH from 2014 to 2016 varied from 49.3 to 57.1 for the forest, 45.1 to 51.6 for the hayfield, and 40.4 to 45.6 W m^{-2} for the cornfield, which were close to the observations of the corresponding types ranging from 52.4 to 56.4, 45.1 to 47.8, and 45.2 to 47.4 W m^{-2} (Table 3). The calculated RRMSE between the simulated and observed annual LH ranged from 1.2% to 5.9%, 0.5% to 1.6%, and 1.0% to 11.3%, for forest, hayfield, and cornfield, respectively (Table 3).

3.1.3. Sensible Heat

The improved model generally captured the seasonal dynamics and magnitudes of SH across the three land use types (Figure 4). Both the simulations and observations showed that the SH was relatively low during the winter and middle to late growing seasons and relatively high during the early growing seasons for the forest. The SH was relatively low during the winters and relatively high during the summers at the hayfield and relatively low during winters and middle growing seasons and relatively high during early and late growing seasons at the cornfield. The R values between the simulations and field observations from 2014 to 2016 ranged from 0.69 to 0.82, 0.54 to 0.76, and 0.70 to 0.82, for the forest, hayfield, and cornfield, respectively. The simulated seasonal dynamics of SH were significantly correlated with the observations in both the calibration and validation years for the studied land use types ($p < 0.0001$), although a few apparent biases appeared (e.g., late May to early June 2014 for forest and early October 2015 for hayfield; Figure 4). The simulated annual SH varied from 23.5 to 31.9, 5.9 to 14.1, and 13.5 to 19.2 W m^{-2}, for the forest, hayfield, and cornfield, respectively, from 2014 to 2016. The observations of the corresponding types varied from 32.8 to 34.8, 6.0 to 9.4, and 16.2 to 21.0 W m^{-2}. The simulations were comparable to the observations, with the calculated RRMSE between the simulated and observed annual SH ranging from 3.2% to 20.0%, 1.6% to 50.1%, and 3.9% to 16.3%, for forest, hayfield, and cornfield, respectively, for those years when the observed annual total SH was available (Table 3). Both the simulations and observations showed that the SH at the hayfield and cornfield was lower than that at the forest (Table 3).

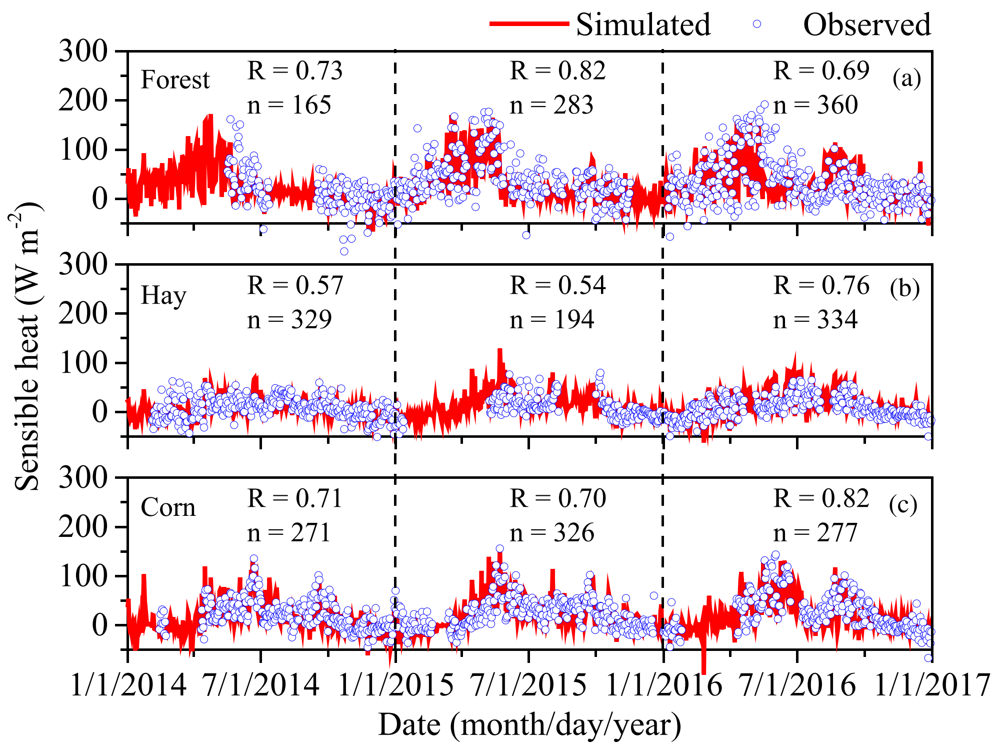

Figure 4. Simulated and observed daily sensible heat fluxes at the (a) forest, (b) hayfield, and (c) cornfield during the period from 2014 to 2016. The correlations between the simulated and observed daily sensible heat fluxes were significant for all cases (P < 0.0001).

3.1.4. Nee

The NEE observations at the forest showed a clear seasonal cycle, with net CO_2 uptake increasing from late spring to early summer, strong net CO_2 uptake for most days during middle summer to early autumn, and net CO_2 release from middle autumn to winter (Figure 5a). In comparison with the measurements, DNDC generally captured the seasonal characteristics and magnitudes of daily NEE. The R values were 0.85 in 2014 (calibration) and were 0.85 and 0.78 in 2015 and 2016, respectively (validation, Figure 5a), indicating that there were strong correlations between the simulated and observed daily NEE for both the calibration and validation years ($P < 0.0001$). The observed annual total NEE were −547.3 and −326.3 g CO_2-C m^{-2}, respectively, in 2015 and 2016, and the simulations were −495.8 and −439.7 g CO_2-C m^{-2}. Sufficient observational data were not available for the calculation of annual NEE in 2014. The calculated RRMSE values were 9.4% and 34.8% for 2015 and 2016, respectively (Table 3).

At the hayfield, the seasonal variations of daily NEE were regulated by both climate and farming management practices. Both the simulations and observations showed that net CO_2 uptake increased in spring and the ecosystem switched to net CO_2 sources in autumn and winter seasons. During summer seasons, net CO_2 release appeared following the events of grass cutting and/or manure amendment, and net CO_2 uptake prevailed on most other days (Figure 5b). The modeled and observed daily NEE was significantly correlated in both the calibration and validation years ($P < 0.0001$), and the R values were 0.72 in 2014 and 0.67 and 0.64 in 2015 and 2016, respectively. These results suggested that the improved DNDC model generally captured the seasonal patterns of daily NEE at the hayfield. The predicted annual total NEE were −193.9, −157.0, and −149.1 g CO_2-C m^{-2}, for 2014, 2015, and 2016, respectively. The observed annual total NEE were −146.7 for 2014 and −119.8 g CO_2-C m^{-2} for 2016. The predictions were comparable to the observations, with the RRMSE values calculated as 32.2% for 2014 and 24.5% for 2016 (Table 3).

At the cornfield, both the simulated and observed daily NEE showed similar seasonal patterns from 2014 to 2016, with net CO_2 uptake increasing following corn planting, strong net CO_2 uptake for most days during corn growing seasons from May to September, and net CO_2 release following corn harvesting (Figure 5c). The R values were 0.74 in 2014 and 0.87 and 0.91 in 2015 and 2016, respectively. The correlations between

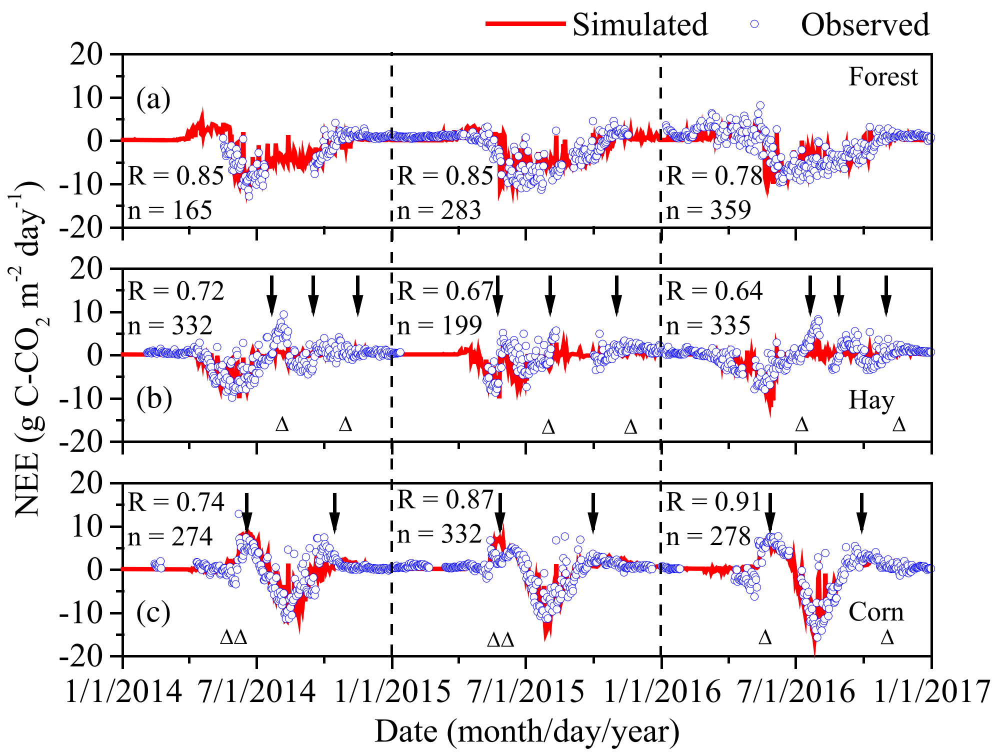

Figure 5. Simulated and observed daily net ecosystem exchange (NEE) of CO_2 at the (a) forest, (b) hayfield, and (c) cornfield during the period from 2014 to 2016. The arrows indicate the dates of cutting events for hayfield and planting and harvest for cornfield. The triangles indicate the dates of manure amendment. The correlations between the simulated and observed daily NEE were significant for all cases ($P < 0.0001$).

the modeled and measured daily NEE were significant ($P < 0.0001$) for both the calibration and validation years. The model also captured the magnitudes of the observed NEE. The simulations of annual total NEE from 2014 to 2016 varied between −50.3 to 52.1 g CO_2-C m^{-2}, which were close to the observations ranging from −47.4 to 48.6 g CO_2-C m^{-2}. The RRMSE values were 7.2% in 2014 and 30.2% and 6.0% in 2015 and 2016, respectively (Table 3).

3.2. Energy and GHG Fluxes of Different Land Use Types

Both the simulations and observations showed that the energy fluxes and NEE were different across the three land use types (Figure 6). The average annual total OSW at the forest was lower than that at the hayfield and cornfield, and the average annual LH and SH at the forest were higher than those at the hayfield and cornfield (Figures 6a to 6c). The mean annual total NEE was also different across the three land use types and showed a trend of forest greater than hayfield greater than cornfield for net CO_2 uptake (Figure 6d). In comparison with the hay and corn sites, the forest reflected less SW but sequestrated more CO_2 and therefore exerted both more climate warming and cooling impacts through different mechanisms over a short-term scale from 2014 to 2016.

The long-term predictions also showed different energy and GHG fluxes at the forest, hayfield, and cornfield. Over the 100-year simulations, annual OSW varied from 20.9 to 24.6 (forest, mean: 22.4), 36.8 to 54.9 (hayfield, mean: 44.3), and 33.4 to 50.3 (cornfield, mean: 43.0) W m^{-2} (Figure 7a). In comparison with the hay or corn site, the forest would continuously have less OSW and exert a stronger warming effect over the simulations (Figure 7a).

The simulations of net CO_2 flux ranged from −518.7 to 105.6 (forest, mean: −181.3), −620.5 to 763.9 (hayfield, mean: −73.1), and −63.6 to 77.2 (cornfield, mean: 10.9) g C-CO_2 m^{-2} $year^{-1}$ (Figure 7b). The forest sequestered CO_2 for most of the simulation years. However, its capacity of sequestrating CO_2 gradually decreased due to limited biomass growth and soil organic carbon increases as the forest becomes older

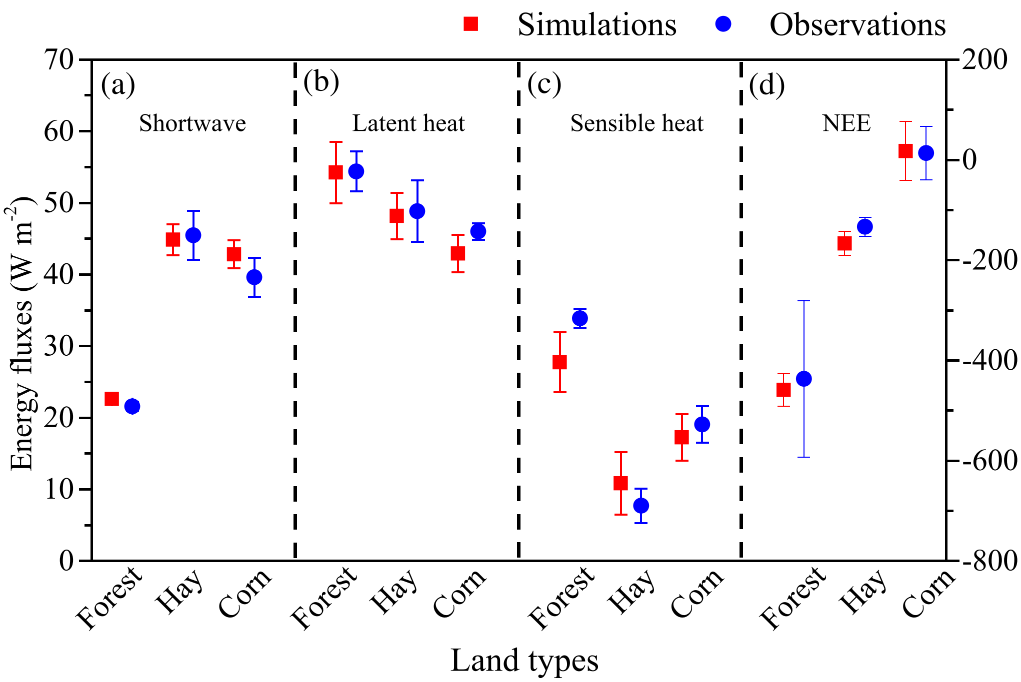

Figure 6. Simulated and observed means of annual total (a) outgoing shortwave, (b) latent heat, (c) sensible heat, and (d) net ecosystem exchange of CO_2 at the forest, hay, and corn sites. Data are means of simulated or observed annual total energy fluxes and NEE from 2004 to 2016 (listed in Table 3). Vertical bars are stand deviations of annual total fluxes and NEE and indicate their interannual variations. Please note that the observed annual total energy fluxes and NEE were not always available due to relatively low data coverage in some years (Table 3).

(Figure 7b). At the hayfield, the model predicted strong interannual variations in net CO_2 flux because different management practices were applied during a hay growth cycle. The net CO_2 flux was a strong net CO_2 sink in years of hay termination because of the C input from root incorporation, a net CO_2 source in years of planting due to increases of soil heterotrophic respiration induced by the root incorporation in previous years with hay termination, and a moderate net CO_2 sink in other years (Figure 7b). For the cornfield, the net CO_2 flux would fluctuate around 0 and generally show less interannual variability in comparison with the forest and hayfield (Figure 7b). Over the simulations, the predicted average and cumulative net CO_2 sequestration was the highest for forest, medium for hayfield, and the lowest for cornfield (Figure 7b).

The long-term simulations showed that all the three land use types would take up CH_4 from the atmosphere and emit N_2O to the atmosphere in each year. The simulations of net CH_4 uptake rate ranged from 0.23 to 0.55 (forest, mean: 0.42), 0.18 to 0.33 (hayfield, mean: 0.26), and 0.20 to 0.28 (cornfield, mean: 0.25) g C-CH_4 m^{-2} $year^{-1}$ (Figure 7c). The simulated CH_4 uptake rate at the forest gradually increased due to the SOM increase that enhanced the microbial activity, soil porosity, and CH_4 diffusivity and thereby increased the CH_4 uptake rate (Castro et al., 1995; Del Grosso et al., 2000). The simulations of N_2O emission ranged from 0.02 to 0.48 (forest; mean: 0.12), 0.03 to 1.71 (hayfield; mean: 0. 26), and 0.39 to 1.98 (cornfield; mean: 1.05) g N-N_2O m^{-2} $year^{-1}$ (Figure 7d). The forest site would uptake more CH_4 and emit less N_2O in comparison with the hay or corn site (Figures 7c and 7d).

The simulations showed that there are tradeoffs between climate cooling and warming impacts among the three dominant land use types in northeastern United States. The forest reflected less SW and therefore exerted a stronger warming effect in comparison with the hayfield or cornfield (Figure 7a and Table 4). The forest also sequestered more CO_2 and CH_4 from the atmosphere and emitted less N_2O compared to hayfield or cornfield and therefore also exerted a stronger cooling effect (Figures 7b to 7d and Table 4). The 100-year simulations further showed that the dynamics of the OSW and GHG fluxes varied among years (Figure 7). For example, every year the forest reflected less SW and exerted a stronger warming impact in comparison with the hayfield or cornfield (Figure 7a). However, its capacity of sequestering CO_2

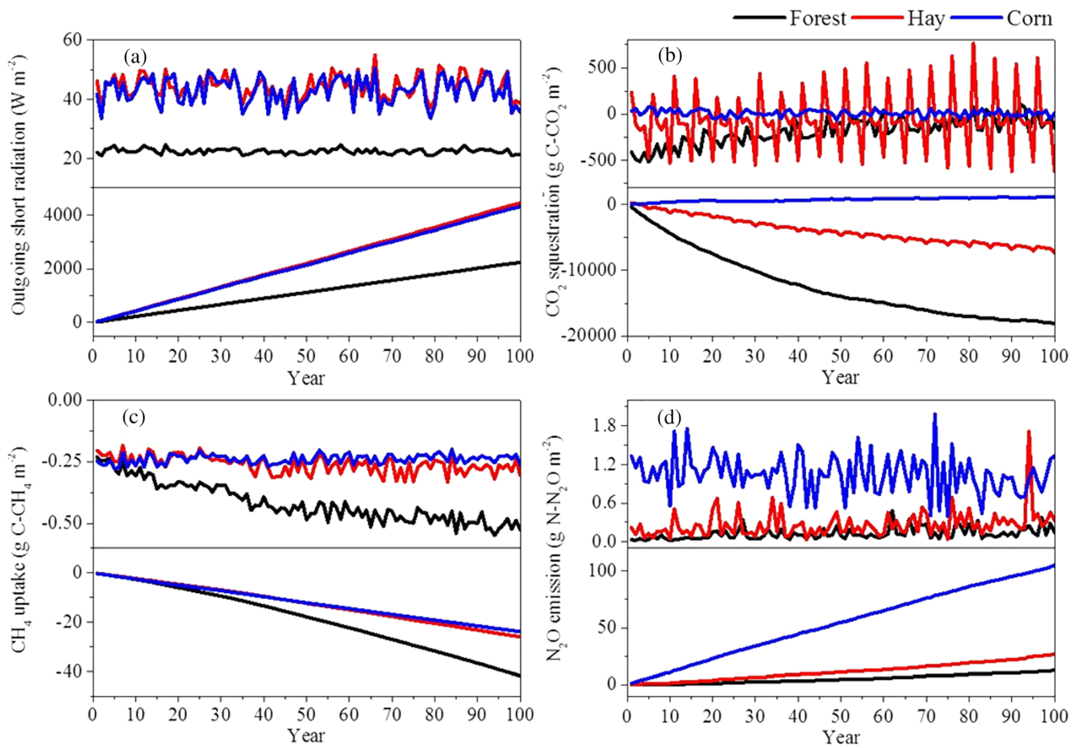

Figure 7. Simulated long-term trends of (a) outgoing shortwave radiation, (b) net CO_2 flux, (c) CH_4 uptake, and (d) N_2O emission at the forest, hay, and corn sites. Data presented are annual simulations (upper part in each panel) and cumulative values of the annual simulations (lower part in each panel).

gradually decreased to a level that is comparable to the cornfield (Figure 7b), suggesting that the stronger GHG cooling effect of the forest through CO_2 sequestration would decline over time.

3.3. Net Radiative Forcing Among Different Land Use Types

The differences in radiative forcing among different land use types (hayfield or cornfield vs. forest), expressed as nanowatt per square meter per hectare land use difference, were calculated by considering the simulated OSW and net GHG fluxes (Figure 8 and Table 4). Compared with the forest, the hayfield or cornfield would reflect more SW and therefore exert a stronger cooling effect (negative values in the differences of radiative forcing for cooling effects) to the Earth's surface. The calculated global cooling effect due to the differences in OSW ranged from −0.45 to −0.22 (mean: −0.31) per hectare of difference between hayfield and forest (i.e., hayfield minus forest) and −0.38 to −0.18 (mean: −0.29) nW m^{-2} per hectare of difference between cornfield and forest (i.e., cornfield minus forest) over the 100-year simulations. The hayfield or cornfield would exert a stronger warming effect (positive values in the differences of radiative forcing for warming effects) primarily through sequestering less CO_2 from the atmosphere (Figure 8). The differences in radiative forcing between the forest and other two land use types were negative during initial simulation years (around 10 years for cornfield and 25 years for hayfield) and increased to a level of fluctuating around to 0 for hayfield or to positive values for cornfield over the 100-year simulations. These results suggested that the cooling effect of the hayfield or cornfield as compared to forest due to the albedo difference would be gradually offset by the warming effect due to the differences in net GHG

Table 4
Radiative Forcing (RF; Unit: nW m^{-2} Per Hectare of Land) Related to Outgoing Shortwave Radiation (OSW) and Greenhouse Gas (GHG) Fluxes and the Differences in RF Among Different Land Use Types

RF	Forest	Hay	Corn	Hay minus forest	Corn minus forest
Radiative forcing related to OSW					
Minimum	−0.35	−0.78	−0.71	−0.45	−0.38
Maximum	−0.30	−0.52	−0.47	−0.22	−0.18
Cumulative RF	−31.7	−62.6	−60.7	−30.9	−29.1
Radiative forcing related to GHG fluxes					
Minimum	−0.54	−0.16	0.01	0.04	0.04
Maximum	−0.03	0.02	0.46	0.43	0.98
Cumulative RF	−44.4	−10.1	28.0	34.3	72.3
Net radiative forcing related to OSW and GHG fluxes					
Minimum	−0.88	−0.89	−0.62	−0.30	−0.24
Maximum	−0.34	−0.51	−0.42	0.19	0.78
Cumulative RF	−76.0	−72.7	−32.8	3.35	43.2

Note. Data presented are minimum and maximum as well as cumulative RF over the 100-year simulations. The average RF equals the cumulative RF divided by 100.

10.1029/2019GB006520

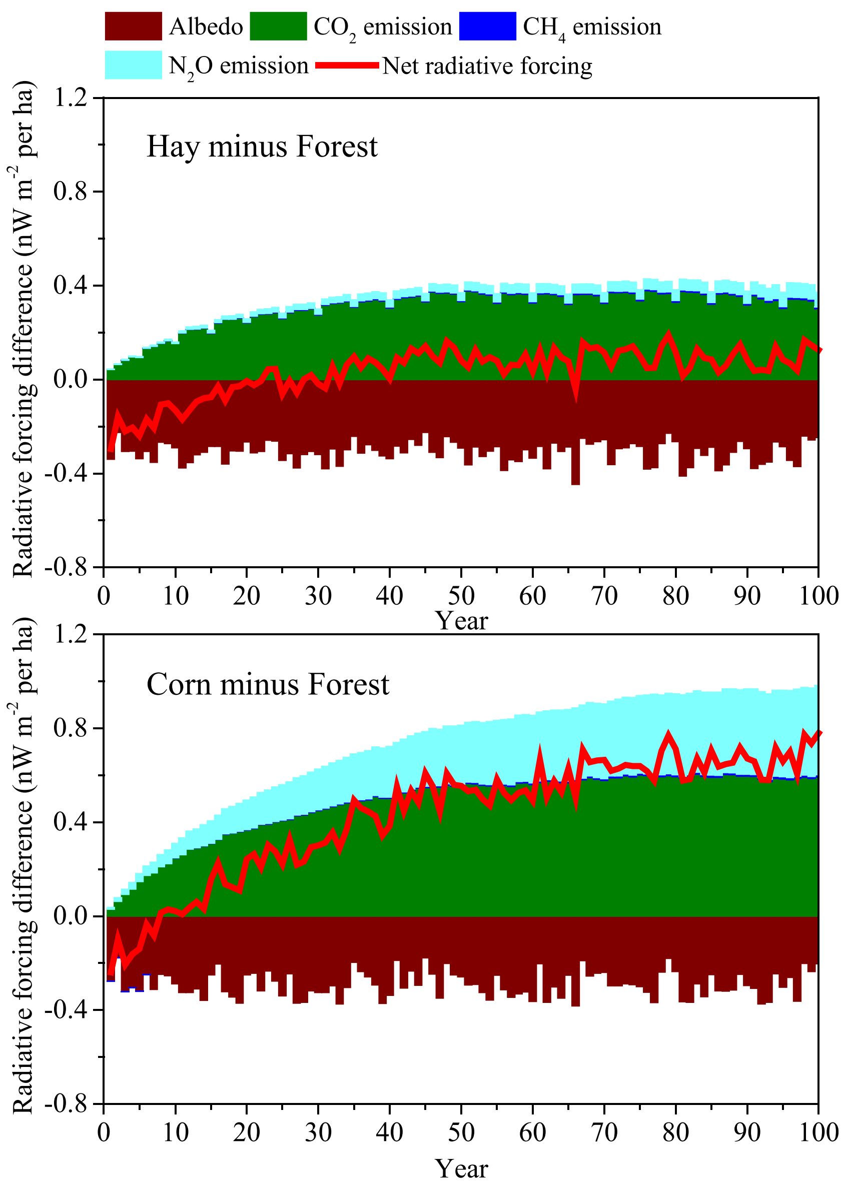

Figure 8. Difference of simulated annual radiative forcing between (a) forest and hayfield (hayfield minus forest) and (b) forest and cornfield (cornfield minus forest). The brown, green, blue, and cyan bars are the differences of radiative forcing from albedo, perturbed atmospheric CO_2, CH_4, and N_2O, respectively, between the studied sites. The red lines are the net differences of radiative forcing by considering albedo and all three GHG. Positive values indicate warming effects and negative values indicate cooling effects.

fluxes. The cumulative differences in net radiative forcing over the 100-year simulations were 3.35 and 43.2 nW m^{-2} per hectare land use difference for hayfield versus forest (net cooling) and cornfield versus forest (net warming), respectively (Table 4).

4. Discussion

4.1. Model Evaluation

In this study, we modified a widely used biogeochemical model—DNDC—by incorporating the processes of surface energy exchange into the model and then applied the model to assess the radiative forcing of the three dominant land use types in the northeastern United States by considering both OSW and GHG fluxes. The modified DNDC provides a framework to quantitatively evaluate radiative forcing from different land uses by simulating both energy fluxes and detailed management practices and biogeochemical processes

10.1029/2019GB006520

related to GHG fluxes. The model was tested against the observed energy fluxes and NEE from the adjacent forest, hayfield, and cornfield. Both the simulations and observations showed that OSW, LH, SH, and NEE were different across these three land use types and the simulated annual energy fluxes and NEE were comparable to the observations. In addition, the model generally captured the observed magnitudes and seasonal dynamics of daily OSW, LH, SH, and NEE. The results from the model tests suggested that the improved DNDC can be used to predict energy and GHG fluxes for the studied land use types although there were some discrepancies between the simulations and observations.

Compared to the daily observations of LH and SH, the model slightly overestimated these fluxes during some periods of vegetation growing seasons (e.g., early forest growing periods, mid-June 2016 for hay, and April 2015 for corn). These discrepancies partially resulted from an energy imbalance problem in the measurements (i.e., net radiation minus ground heat flux is greater than the sum of LH and SH at many eddy flux sites) (e.g., Wilson et al., 2002). Because the simulated energy fluxes do not have the energy imbalance issue while the field measurements have this issue, the simulated daily LH and SH could be higher than the observations in this study. The discrepancies may also result from inaccurate parameterization of the model. For instance, specific leaf area may vary across different periods within a growing season depending on leaf development stage, soil water, and nutrient conditions (e.g., Tardieu et al., 1999), although it has been simplified to one value during the entire growing season. This simplification may lead to biases in the prediction of seasonal dynamics of leaf area index and subsequently of energy fluxes.

The improved DNDC model predicted less CO_2 release rates during the late winter to early spring in 2016 at the forest. The high observed CO_2 release rates in this period were likely due to anomalously warm conditions in the winter of 2015/2016 (NOAA National Centers for Environmental Information, 2017) and relatively high temperature sensitivities of ecosystem respiration ($Q_{10} \approx 3.6$ to 4.7) during the winter to spring period at the forest that led to warm soil conditions and high CO_2 release rates (Sanders-DeMott et al., 2019). However, since DNDC integrated equations with lower temperature sensitivities for ecosystem respiration (Li et al., 1992a), the model predicted lower daily NEE values. The underestimation of the CO_2 release rate during this period resulted in the overestimation of the annual total CO_2 uptake in 2016. At the cornfield, the model underestimated NEE on a few days during the growing seasons (e.g., 13 August 2014, 23 August 2015, and 10 August 2016). Solar radiation was relatively low on these days, and therefore, the field observations showed positive NEE values due to constrained photosynthesis. Although the improved DNDC model captured the NEE increases, it underestimated the reduction in photosynthesis due to low solar radiation on these days, causing the model to predict higher NPP and thereby negative or less positive NEE. The model also underestimated NEE following the hay cutting events in summers although it captured the increases of NEE following these events. These discrepancies could be due to the overestimated photosynthesis or underestimated ecosystem respiration following these cutting events. Further studies are needed to clarify the discrepancies between the simulations and observations.

In addition, it should be noted that there are significant uncertainties in the eddy-covariance measurements of LH, SH, and NEE due to uncertainties associated with the instrument, source heterogeneity, gap-filling, and the turbulent nature of the transport process (Falge et al., 2001; Mauder et al., 2013; Richardson et al., 2006). The uncertainties of the measurements can also contribute to the discrepancies between simulated and measured energy fluxes and NEE. For example, Mauder et al. (2013) estimated that random measurement errors were around 20% to 30% of the LH, SH, and NEE values at several sites with different land uses (forest, grassland, and cropland). These measurement uncertainties are larger than or comparable to the discrepancies between the simulated and measured annual total LH, SH, and NEE for most of the testing site-year combinations in this study.

4.2. Net Radiative Forcing Among Different Land Use Types

The model predictions show how radiative forcing differs among different land uses in the study region. Both the hayfield and cornfield reflect more SW radiation than forest. Therefore, if the landscape configuration of the northeastern United States had less forest and more hayfield or cornfield, more SW could be reflected, especially during snow seasons (Zhao & Jackson, 2014). The global cooling effect due to the increases of OSW ranged from −0.45 to −0.22 (mean: −0.31) nW m^{-2} per hectare of the difference between forest and hayfield and −0.38 to −0.18 (mean: −0.29) nW m^{-2} per hectare of the difference between forest and cornfield. These results are similar in magnitudes to the estimates by Jones et al. (2015) who reported a net cooling of around -0.40 nW m^{-2} due to land conversion from forest or shrub to grass or crop in the northeastern United States.

However, the hayfield and cornfield were predicted to sequester less CO_2 primarily because the C in harvested biomass would be released to the atmosphere soon (within 1 or 2 years via consumption) and we assumed that there is no forest harvest or major disturbance (e.g., fire) during the 100-year simulation. Therefore, the hay and corn sites also exert a stronger warming effect than the forest through sequestering less or releasing more GHG. The cooling effect due to the increasing OSW would be counteracted by the warming effect due to the increasing GHG release along with the land cover change from forest to hayfield or cornfield. Although the warming effect due to the GHG differences would be smaller than the cooling effect due to the albedo differences during the initial simulation years, it would increase, and the net effects would be close to neutral for the hayfield and consistently warming the global climate for the cornfield after the initial simulation years. The calculated effects by comparing the forest and hayfield are in line with the study by Kirschbaum et al. (2011) who reported increasing radiative effects due to GHG differences between forest and pasture as the forest grew older, although they only analyzed differences in albedo and C without consideration of CH_4 or N_2O. However, the differences in N_2O flux exerted relatively large contributions to the differences in radiative forcing between cornfield and forest (Figure 8) primarily due to the relatively large N_2O emissions at the cornfield (Figure 7), indicating that it may be important to consider N_2O flux when estimating the radiative forcing between different land uses, in particular for lands with large N_2O flux. The cumulative difference in radiative forcing between cornfield and forest was substantially higher than that between hayfield and forest primarily due to the different farming management practices applied and thereby net CO_2 and N_2O emissions in the hayfield and cornfield. The simulations further demonstrate that relatively short (e.g., less than 10 years) and long time span (e.g., around 100 years) of different land use had contrasting impacts on the climate, suggesting that the estimation of the radiative forcing to climate due to the land use differences needs to consider the timescale of investigation period.

It should be noted that there are uncertainties in the long-term simulations of energy and GHG fluxes because the model was only evaluated against short-term (3 years) observations of energy fluxes and NEE due to limited data availability. The simulated CH_4 fluxes were relatively low at all sites and made a small contribution to overall radiative forcing. Uncertainties in the simulations of CH_4 will have a small influence on the radiative forcing due to its relatively small contribution to the total. These simulated low CH_4 fluxes are generally consistent with field measurements from upland forests, hayfields, and corn fields (Dutaur & Verchot, 2007). On the other hand, uncertainties in forest NEE and N_2O flux at the cornfield may have a large influence due to their relatively large contributions to total radiative forcing (Figure 8). However, the simulated NEE is broadly consistent with previous studies that generally identified forests as C sinks in the northeastern United States (e.g., Williams et al., 2012). In addition, the NEE results are generally comparable with the observed NEE for similar forests in the study region. For example, the simulations of NEE (range: -520 to 110 g C-CO_2 m^{-2} $year^{-1}$; mean: -180 g C-CO_2 m^{-2} $year^{-1}$) over the 100-year simulations were comparable with the NEE based on decadal observations (range: -470 to -100 g C-CO_2 m^{-2} $year^{-1}$; mean: -250 g C-CO_2 m^{-2} $year^{-1}$) for a mixed deciduous forest in the northeastern United States (Urbanski et al., 2007). The variations of the simulated NEE were larger than the observations, probably due to the longer timescale for the simulations. Furthermore, the simulated increase in forest biomass is comparable with the previous estimates. For example, annual aboveground wood growth rate was measured ranging from about 140 to 320 g C m^{-2} $year^{-1}$ between 2005 and 2016 for a mixed deciduous forest in the study region (Ouimette et al., 2018). The results are close to the simulated wood growth rate ranging from 155 to 290 g C m^{-2} $year^{-1}$ during the same period.

In addition to forest NEE, the simulated relatively large N_2O emissions at the cornfield (range: 0.39 to 1.98 g N-N_2O m^{-2} $year^{-1}$ or 1.0% to 5.2% of the N applied; mean: 1.05 g N-N_2O m^{-2} $year^{-1}$ or 2.8% of the N applied) exerted a large influence on the differences in radiative forcing between the forest and cornfield. The simulated large N_2O emissions at the cornfield were primarily due to the applications of the synthetic fertilizer and slurry manure; this provided both readily available C and N for N_2O production and thereby enhanced the N_2O emission. The simulated N_2O emissions were also comparable with the study by Decock (2014) who reported that about 0.4% to 11.1% (mean: 2.9%) of the N applied through liquid manure was released as N_2O across cornfields in the Midwestern United States and southeast Canada. There is no long-term study that quantified N_2O emissions from cornfields in the study region, but the strong dependence of N_2O emissions on short-term management (i.e., fertilizer and slurry manure) means that long-term behavior will be primarily dependent on long-term management activity, not changes in the cornfield itself.

In addition, there are uncertainties regarding the net impacts of ecosystems on climate for the studied land use types because radiative forcing is not able to represent the full impact of land use change. For example, we only focused on the impacts at the global scale although the albedo change has stronger impacts on regional climate than the change of GHG flux, as GHGs are long-lived, well-mixed gases that affect radiative forcing globally. In addition, both the simulations and observations indicated that the partitions of available energy into LH and SH were different among the forest, hayfield, and cornfield. The partitioning does not directly affect radiative forcing to climate and the simulated GHG fluxes; the latter are primarily driven by plant growth and/or biogeochemical processes (e.g., decomposition, nitrification, and denitrification) in DNDC. However, it exerts a direct impact on near-surface air temperature, cloud cover, and/or water vapor concentration (e.g., Findell et al., 2007; Kirschbaum et al., 2011; Zhao & Jackson, 2014). Therefore, a change in this partitioning should be considered when evaluating net impacts of land use changes on climate. Although the partitioning does not exert direct impact on radiative forcing and quantifying the impacts is beyond the capability of biogeochemical models, such as DNDC, future studies should quantify the impacts due to the different partitions of available energy into LH and SH.

It is important to note that the assessments on the climate effect due to the land use change were based on the comparisons of the OSW, GHG fluxes, and radiative forcing among the three land use types. We did not explicitly simulate the conversion from forest to hayfield or cornfield, along with the resulting transient changes in energy and GHG fluxes. Such simulations would require detailed local management information (such as deforestation time and method, wood utilization, land preparation, and tillage) during the land use conversions. Therefore, the assessments of the climate impacts in this study do not represent the full climate impacts of the land use change, and they are not sufficient for designing land management to mitigate climate change. In order to investigate impacts of forest management on the differences in radiative forcing among the three land use types, we created a scenario with intensive forest harvest, with 90% of the forest biomass C harvested and released as CO_2 to the atmosphere in simulation year of 80 and calculated the differences in the radiative forcing among the three land use types by considering both OSW and GHG fluxes. Because of the pulse release of forest biomass C, the differences in radiative forcing switched to negative values in the forest harvest year for both hayfield versus forest and cornfield versus forest (Figure S1 in the supporting information). The cumulative differences in net radiative forcing over the 100-year simulations were reduced from 3.35 to -10.9 nW m^{-2} and from 43.2 to 29.0 nW m^{-2} per hectare land use difference, for hayfield versus forest (changing from slightly warming to cooling for the hayfield with forest biomass C release) and cornfield versus forest (less warming for the cornfield with forest biomass C release), respectively. These results highlighted the importance of forest management for the differences in the radiative forcing among the three land use types. Previous studies also reported that forest management could be critical for the assessment on the impacts of land use change on climate (Fahey et al., 2010; Lippke et al., 2011; Nunery & Keeton, 2010). Therefore, further studies need to simulate the conversion of forest to hayfields or cornfields by accounting for activities during the transition of land use change.

5. Conclusions

We incorporated processes of surface energy exchange into a widely used biogeochemistry model, DNDC. By including these features, DNDC can simulate both GHG and energy fluxes between soil, vegetation, and the atmosphere. The improved model was evaluated against energy fluxes and NEE observed from the forest, hay, and crop sites in northeastern United States. The model evaluations demonstrated that the improved DNDC successfully captured the differences in OSW, LH, SH, and NEE among the three land use types. Both the simulations and observations demonstrated that the forest reflected less shortwave radiation but sequestrated more CO_2 than the adjacent hay or crop, suggesting that forest may exert both stronger global warming and cooling effects to the Earth's surface. We further evaluated differences in radiative forcing among these land use types by conducting 100-year DNDC simulations and linking the predictions of

OSW and GHG fluxes with an atmospheric impulse response model. The results suggested that the differences in radiative forcing between the forest and other two land use types were negative during initial simulation years and would generally increase to a level of fluctuating around 0 for hay or to positive values for corn over the 100-year simulations. Therefore, the cooling effect of the hayfield or cornfield as compared to forest due to the albedo difference would be gradually offset by the warming effect due to the differences in net GHG fluxes. The accumulative differences in net radiative forcing over the 100-year simulations were 3.35 and 43.2 nW m^{-2} per hectare land use difference for hayfield versus forest (slight warming) and cornfield versus forest (warming), respectively.

Appendix A: Key Equations to Simulate Energy Fluxes Between Soil, Vegetation, and the Atmosphere

Equations A0 to A27 in Appendix A are key equations to simulate energy fluxes between soil, vegetation, and the atmosphere

Equations		
Energy fluxes of canopy		Notes
(A1)	$L_v + S_v = H_v + \lambda E_v + C_v * \mathrm{d}T_v/\mathrm{d}t$	Energy balance of the canopy
(A2)	$L_v = \alpha_v * (\sigma * \varepsilon_a * T_a{}^4 + L_g\uparrow) - 2 * \sigma * \varepsilon_v * T_v{}^4$	Net longwave radiation absorbed by canopy
(A3)	$L_g\uparrow\ = (1-\varepsilon_g) * L_v\downarrow + \sigma * \varepsilon_g * T_g{}^4$	Upward longwave radiation from the ground surface
(A4)	$L_v\downarrow\ = (1-\varepsilon_v) * \sigma * \varepsilon_a * T_a{}^4 + \sigma * \varepsilon_v * T_v{}^4$	Downward longwave radiation below vegetation
(A5)	$S_v = S * (1-\alpha) * (1 - \exp(-K * LAI))$	Net solar radiation absorbed by vegetation
(A6)	$S_{nv} = L_v + S_v$	Net radiation on the canopy
(A7)	$H = \rho_a * C_{pa} * (T_{va} - T_a)/r_{va} = H_v + H_g$	Net sensible heat flux from vegetation and soil system
(A8)	$H_v = \rho_a * C_{pa} * (T_v - T_{va}) * VAI/r_b$	Sensible heat flux from vegetation
(A9)	$T_{va} = \dfrac{T_a/r_{va} + T_g/r_{gv} + T_v{*}VAI/r_b}{1/r_{va} + 1/r_{gv} + VAI/r_b}$	Canopy air temperature
(A10)	$\lambda E_v = \dfrac{\Delta{*}(S_{nv} - G) + \rho_a{*}C_{pa}{*}VPD/r_{va}}{\Delta + \gamma{*}(1 + r_c/r_{va})}$	Latent heat flux from vegetation
(A11)	$r_{va} = \dfrac{\ln((Z - Z_d)/Z_{om}){*}\ln((Z - Z_d)/Z_{oh})}{k^2 u}{*}(1+\delta)^{\varepsilon}$	Aerodynamic resistance between canopy and the atmosphere
(A12)	$\delta = \dfrac{5{*}g{*}z{*}(T_b - T_a)}{T_a{*}u^2}$	
(A13)	$\varepsilon = \begin{cases} -2 & (\delta \le 0) \\ -0.75 & (\delta > 0) \end{cases}$	
(A14)	$r_b = 100 * (u_v/0.04)^{-1/2}$	Leaf boundary layer resistance
(A15)	$r_{gv} = \dfrac{Z_c{*}\exp(\alpha)}{\alpha{*}K(Z_c)}{*}[\exp(-\alpha{*}Z_o/Z_c) - \exp(-\alpha{*}(Z_d + Z_{oh})/Z_c)]$	Aerodynamic resistance between ground and canopy
(A16)	$K(Z_c) = \dfrac{k^2{*}(Z_c - Z_d){*}u}{\ln((Z_c - Z_d)/Z_{oh})}$	
Energy fluxes of ground surface		
(A17)	$L_g + S_g = H_g + \lambda E_g + G_s$	Energy balance of the ground surface
(A18)	$L_g = \alpha_g * L_v\downarrow\ - \sigma * \varepsilon_g * T_g{}^4$	Net longwave radiation absorbed by ground
(A19)	$S_g = S * (1-\alpha) * \exp(-K * LAI)$	Net solar radiation absorbed by ground
(A20)	$\alpha = \alpha_{snow} * f_{snow} + \alpha_{soil} * (1 - f_{snow})$	
(A21)	$\alpha_{snow} = 0.5 + 0.35 * \exp(-S_{age}/5)$	
(A22)	$f_{snow} = \begin{cases} S_{depth}/0.01 & (S_{depth} < 0.01) \\ 1.0 & (S_{depth} \ge 0.01) \end{cases}$	
(A23)	$S_{ng} = L_g + S_g$	Net radiation on the ground
(A24)	$H_g = \rho_a * C_{pa} * (T_g - T_{va})/r_{gv}$	Sensible heat flux from ground
(A25)	$\lambda E_g = \dfrac{\Delta{*}(S_{ng} - G_s) + \rho_a{*}C_{pa}{*}VPD/r_{gv}}{\Delta + \gamma{*}(1 + r_s/r_{gv})}$	Latent heat flux from ground
(A26)	$r_s = 30.0 + 3.5 * (SW)^{-2.3}$	Surface resistance for evaporation
(A27)	$G_s = k_1 * (T_g - T_1)/(0.5 * D_1)$	Ground heat flux

10.1029/2019GB006520

Appendix B: Definitions of Variables Listed in Appendix A

Definitions of relevant variables are listed in Appendix B

Variables	Definition
C_{pa}	Specific heat capacity of air at constant pressure (J kg^{-1} K^{-1})
Cv	Heat capacity of canopy in a unit area (J m^{-2} K^{-1})
D_1	Thickness of the first snow or soil layer (m)
λE_g	Latent heat flux from ground (W m^{-2})
λE_v	Latent heat flux from vegetation (W m^{-2})
g	Gravitational acceleration (9.8 m s^{-2})
G_s	Ground heat flux (W m^{-2})
H	Net sensible heat flux from vegetation and soil system (W m^{-2})
H_g	Sensible heat flux from ground (W m^{-2})
H_v	Sensible heat flux from vegetation (W m^{-2})
k	Von Kármán constant, 0.41
k_1	Thermal conductivity of the top layer (W m^{-1} °C^{-1})
K	Extinction coefficient of solar radiation in canopy
L_g	Net longwave radiation absorbed by ground (W m^{-2})
$L_g\uparrow$	Upward longwave radiation from ground (W m^{-2})
L_v	Net longwave radiation absorbed by vegetation (W m^{-2})
$L_v\downarrow$	Downward longwave radiation below vegetation (W m^{-2})
r_b	Leaf boundary layer resistance (s m^{-1})
r_{gv}	Aerodynamic resistance between ground and canopy air (s m^{-1})
r_s	Soil resistance for evaporation (s m^{-1})
r_{va}	Aerodynamic resistance between canopy and the air above the canopy (s m^{-1})
S	Incident solar radiation above the canopy (W m^{-2})
S_{age}	Age of surface snow
S_{depth}	Snow depth
S_g	Net solar radiation absorbed by ground (W m^{-2})
S_{ng}	Net radiation on the ground (W m^{-2})
S_{nv}	Net radiation on the canopy (W m^{-2})
S_v	Net solar radiation absorbed by vegetation (W m^{-2})
SW	Soil moisture of the surface soil layer, water-filled pore space
T_1	Temperature of the surface snow or soil layer (°C)
T_a	Air temperature above the canopy (K)
T_g	Surface temperature of the ground (no snow) or snowpack (K)
T_v	Canopy temperature (K)
T_{va}	Canopy air temperature (K)
u	Wind speed above the canopy (m S^{-1})
u_v	Wind speed within the canopy (m S^{-1})
VAI	Vegetation area index (m^2 m^{-2})
VPD	Vapor pressure deficit (mbar)
Z	Reference height of measurements (m)
Z_c	Canopy height (m)
Z_d	Zero plane displacement of the canopy or ground surface (m)
Z_o	Roughness length of the ground surface (m)
Z_{oh}	Roughness length governing momentum transfer for the canopy (m)
Z_{om}	Roughness length governing heat and vapor transfer for the canopy (m)
α	Albedo
α_{snow}	Snow albedo
α_{soil}	Soil albedo
α_g, α_v	Absorption capability of ground and vegetation and equals to ε_g and ε_v, respectively
γ	Psychrometer constant (J kg^{-1} K^{-1})
ε_a, ε_g, ε_v	Emissivity of air, soil or snow surface, and vegetation, respectively
ρ_a	Air density (kg m^{-3})
σ	Stefan-Boltzman constant (5.7 × 10^{-8} W m^{-2} K^{-4})
Δ	Change rate of saturation vapor pressure with temperature (mbar K^{-1})

Data Availability Statement

The DNDC model, model input files, and all data used in this study are archived at Institute for the Study of Earth, Oceans, and Space, University of New Hampshire (ftp://ftp.eos.sr.unh.edu/pub/outgoing/Li/Data%20Package%20for%20Energy,%20GHG,%20and%20RF%20in%20NE%20USA/).

Acknowledgments
This research was supported by National Aeronautics and Space Administration (NASA) through the Carbon Cycle Science Program (Grant NNX14AJ18G). It was also partly funded by NASA's Interdisciplinary Research in Earth Science (Grant NNX17AK10G) and Climate Indicators and Data Products for Future National Climate Assessments (Grant NNX16AG61G) and USDA National Institute of Food and Agriculture (Grant 2016-68002-24967). We thank two anonymous reviewers for comments and suggestions that improved the manuscript.

References

Bell, J. E., Palecki, M. A., Baker, C. B., Collins, W. G., Lawrimore, J. H., Leeper, R. D., et al. (2013). US Climate Reference Network soil moisture and temperature observations. *Journal of Hydrometeorology*, *14*(3), 977–988. https://doi.org/10.1175/JHM-D-12-0146.1

Betts, R. A. (2000). Offset of the potential carbon sink from boreal forestation by decreases in surface albedo. *Nature*, *408*(6809), 187–190. https://doi.org/10.1038/35041545

Bolinder, M. A., Janzen, H. H., Gregorich, E. G., Angers, D. A., & VandenBygaart, A. J. (2007). An approach for estimating net primary productivity and annual carbon inputs to soil for common agricultural crops in Canada. *Agriculture, Ecosystems & Environment*, *118*(1–4), 29–42. https://doi.org/10.1016/j.agee.2006.05.013

Bonan, G. B. (2008). Forests and climate change: Forcings, feedbacks, and the climate benefits of forests. *Science*, *320*(5882), 1444–1449. https://doi.org/10.1126/science.1155121

Brovkin, V., Claussen, M., Driesschaert, E., Fichefet, T., Kicklighter, D., Loutre, M. F., et al. (2006). Biogeophysical effects of historical land cover changes simulated by six Earth system models of intermediate complexity. *Climate Dynamics*, *26*(6), 587–600. https://doi.org/10.1007/s00382-005-0092-6

Burakowski, E., Tawfik, A., Ouimette, A., Lepine, L., Novick, K., Ollinger, S., et al. (2018). The role of surface roughness, albedo, and Bowen ratio on ecosystem energy balance in the Eastern United States. *Agricultural and Forest Meteorology*, *249*(15), 367–376. https://doi.org/10.1016/j.agrformet.2017.11.030

Campbell, G. S., & Norman, J. M. (Eds.). (2012). *An introduction to environmental biophysics*. New York, NY: Springer-Verlag.

Castro, M. S., Steudler, P. A., Melillo, J. M., Aber, J. D., & Bowden, R. D. (1995). Factors controlling atmospheric methane consumption by temperate forest soils. *Global Biogeochemical Cycles*, *9*(1), 1–10. https://doi.org/10.1029/94GB02651

Choudhury, B. J., & Monteith, J. L. (1988). A four-layer model for the heat budget of homogeneous land surfaces. *Quarterly Journal of the Royal Meteorological Society*, *114*(480), 373–398. https://doi.org/10.1002/qj.49711448006

Cox, P. M., Betts, R. A., Bunton, C. B., Essery, R. L. H., Rowntree, P. R., & Smith, J. (1999). The impact of new land surface physics on the GCM simulation of climate and climate sensitivity. *Climate Dynamics*, *15*(3), 183–203. https://doi.org/10.1007/s003820050276

Curtis, P. G., Slay, C. M., Harris, N. L., Tyukavina, A., & Hansen, M. C. (2018). Classifying drivers of global forest loss. *Science*, *361*(6407), 1108–1111. https://doi.org/10.1126/science.aau3445

Dale, V. H. (1997). The relationship between land-use change and climate change. *Ecological Applications*, *7*(3), 753–769. https://doi.org/10.1890/1051-0761(1997)007[0753:TRBLUC]2.0.CO;2

Decock, C. (2014). Mitigating nitrous oxide emissions from corn cropping systems in the Midwestern US: Potential and data gaps. *Environmental Science & Technology*, *48*(8), 4247–4256. https://doi.org/10.1021/es4055324

Deng, J., McCalley, C. K., Frolking, S., Chanton, J., Crill, P., Varner, R., et al. (2017). Adding stable carbon isotopes improves model representation of the role of microbial communities in peatland methane cycling. *Journal of Advances in Modeling Earth Systems*, *9*, 1412–1430. https://doi.org/10.1002/2016MS000817

Diamond, H. J., Karl, T. R., Palecki, M. A., Baker, C. B., Bell, J. E., Leeper, R. D., et al. (2013). US Climate Reference Network after one decade of operations: Status and assessment. *Bulletin of the American Meteorological Society*, *94*(4), 485–498. https://doi.org/10.1175/BAMS-D-12-00170.1

Dutaur, L., & Verchot, L. V. (2007). A global inventory of the soil CH_4 sink. *Global Biogeochemical Cycles*, *21*, GB4013. https://doi.org/10.1029/2006GB002734

Fahey, T. J., Woodbury, P. B., Battles, J. J., Goodale, C. L., Hamburg, S. P., Ollinger, S. V., & Woodall, C. W. (2010). Forest carbon storage: Ecology, management, and policy. *Frontiers in Ecology and the Environment*, *8*(5), 245–252. https://doi.org/10.1890/080169

Falge, E., Baldocchi, D., Olson, R., Anthoni, P., Aubinet, M., Bernhofer, C., et al. (2001). Gap filling strategies for long term energy flux data sets. *Agricultural and Forest Meteorology*, *107*(1), 71–77. https://doi.org/10.1016/S0168-1923(00)00235-5

Feddema, J. J., Oleson, K. W., Bonan, G. B., Mearns, L. O., Buja, L. E., Meehl, G. A., & Washington, W. M. (2005). The importance of land-cover change in simulating future climates. *Science*, *310*(5754), 1674–1678. https://doi.org/10.1126/science.1118160

Findell, K. L., Shevliakova, E., Milly, P. C. D., & Stouffer, R. J. (2007). Modeled impact of anthropogenic land cover change on climate. *Journal of Climate*, *20*(14), 3621–3634. https://doi.org/10.1175/JCLI4185.1

Frolking, S., Roulet, N., & Fuglestvedt, J. (2006). How northern peatlands influence the Earth's radiative budget: Sustained methane emission versus sustained carbon sequestration. *Journal of Geophysical Research*, *111*, G01008. https://doi.org/10.1029/2005JG000091

Frolking, S., & Roulet, N. T. (2007). Holocene radiative forcing impact of northern peatland carbon accumulation and methane emissions. *Global Change Biology*, *13*(5), 1079–1088. https://doi.org/10.1111/j.1365-2486.2007.01339.x

Gilhespy, S. L., Anthony, S., Cardenas, L., Chadwick, D., del Prado, A., Li, C., et al. (2014). First 20 years of DNDC (DeNitrification DeComposition): Model evolution. *Ecological Modelling*, *292*(24), 51–62. https://doi.org/10.1016/j.ecolmodel.2014.09.004

Giltrap, D. L., Li, C., & Saggar, S. (2010). DNDC: A process-based model of greenhouse gas fluxes from agricultural soils. *Agriculture, Ecosystems & Environment*, *136*(3–4), 292–300. https://doi.org/10.1016/j.agee.2009.06.014

Grosso, S. D., Parton, W. J., Mosier, A. R., Ojima, D. S., Potter, C. S., Borken, W., et al. (2000). General CH_4 oxidation model and comparisons of CH_4 oxidation in natural and managed systems. *Global Biogeochemical Cycles*, *14*, 103763101. https://doi.org/10.1029/1999GB001226

Hansen, J., Russell, G., Rind, D., Stone, P., Lacis, A., Lebedeff, S., et al. (1983). Efficient three-dimensional global models for climate studies: Models I and II. *Monthly Weather Review*, *111*(4), 609–662. https://doi.org/10.1175/1520-0493(1983)111<0609:ETDGMF>2.0.CO;2

Hollinger, D. Y., Ollinger, S. V., Richardson, A. D., Meyers, T. P., Dail, D. B., Martin, M. E., et al. (2010). Albedo estimates for land surface models and support for a new paradigm based on foliage nitrogen concentration. *Global Change Biology*, *16*(2), 696–710. https://doi.org/10.1111/j.1365-2486.2009.02028.x

Intergovernmental Panel on Climate Change (2014). In *Climate change 2013: The physical science basis. Contribution of Working Group I to the Fifth Assessment Report of the Intergovernmental Panel on Climate Change* (Chap. 8., pp. 659–740). Cambridge, UK, and New York, NY: Cambridge University Press.

Jeon, S. B., Olofsson, P., & Woodcock, C. E. (2013). Land use change in New England: A reversal of the forest transition. *Journal of Land Use Science*, *9*(1), 105–130.

Jones, A. D., Calvin, K. V., Collins, W. D., & Edmonds, J. (2015). Accounting for radiative forcing from albedo change in future global land-use scenarios. *Climatic Change*, *131*(4), 691–703. https://doi.org/10.1007/s10584-015-1411-5

Kirschbaum, M. U. F., Whitehead, D., Dean, S. M., Beets, P. N., Shepherd, J. D., & Ausseil, A. G. (2011). Implications of albedo changes following afforestation on the benefits of forests as carbon sinks. *Biogeosciences*, *8*(12), 3687–3696. https://doi.org/10.5194/bg-8-3687-2011

Li, C., Aber, J., Stange, F., Butterbach-Bahl, K., & Papen, H. (2000). A process-oriented model of N_2O and NO emissions from forest soils: 1. Model development. *Journal of Geophysical Research*, *105*, 4369–4384. https://doi.org/10.1029/1999JD900949

Li, C., Frolking, S., & Frolking, T. A. (1992a). A model of nitrous oxide evolution from soil driven by rainfall events: 1. Model structure and sensitivity. *Journal of Geophysical Research*, *97*, 9759–9776. https://doi.org/10.1029/92JD00509

Li, C., Frolking, S., & Frolking, T. A. (1992b). A model of nitrous oxide evolution from soil driven by rainfall events: 2. Model applications. *Journal of Geophysical Research*, *97*, 9777–9783. https://doi.org/10.1029/92JD00510

Li, C., Salas, W., Zhang, R., Krauter, C., Rotz, A., & Mitloehner, F. (2012). Manure-DNDC: A biogeochemical process model for quantifying greenhouse gas and ammonia emissions from livestock manure systems. *Nutrient Cycling in Agroecosystems*, *93*(2), 163–200. https://doi.org/10.1007/s10705-012-9507-z

Li, C. S. (2000). Modeling trace gas emissions from agricultural ecosystems. *Nutrient Cycling in Agroecosystems*, *58*(1/3), 259–276. https://doi.org/10.1023/A:1009859006242

Lippke, B., Oneil, E., Harrison, R., Skog, K., Gustavsson, L., & Sathre, R. (2011). Life cycle impacts of forest management and wood utilization on carbon mitigation: Knowns and unknowns. *Carbon Management*, *2*(3), 303–333. https://doi.org/10.4155/cmt.11.24

Liu, J., Chen, J. M., Cihlar, J., & Chen, W. (1999). Net primary productivity distribution in the BOREAS region from a process model using satellite and surface data. *Journal of Geophysical Research*, *104*(D22), 27,735–27,754. https://doi.org/10.1029/1999JD900768

Markvart, T., & Castañer, L. (Eds.). (2003). *Practical handbook of photovoltaics: Fundamentals and applications*. Amsterdam: Elsevier.

Mauder, M., Cuntz, M., Drüe, C., Graf, A., Rebmann, C., Schmid, H. P., et al. (2013). A strategy for quality and uncertainty assessment of long-term eddy-covariance measurements. *Agricultural and Forest Meteorology*, 169(15), 122–135.

Monteith, J. L. (1965). Evaporation and environment. In *Symposia of the Society for Experimental Biology* (pp. 205–234). Cambridge, UK: Cambridge University Press.

Moore, C. J., & Fisch, G. (1986). Estimating heat storage in Amazonian tropical forest. *Agricultural and Forest Meteorology*, *38*(1–3), 147–168. https://doi.org/10.1016/0168-1923(86)90055-9

Moriasi, D. N., Arnold, J. G., Van Liew, M. W., Bingner, R. L., Harmel, R. D., & Veith, T. L. (2007). Model evaluation guidelines for systematic quantification of accuracy in watershed simulations. *Transactions of the ASABE*, *50*(3), 885–900. https://doi.org/10.13031/2013.23153

NOAA National Centers for Environmental Information (2010). NOAA's U.S. Climate Normals (1981–2010). Retrieved from https://data.nodc.noaa.gov/cgi-bin/iso?id=gov.noaa.ncdc: C00824#

NOAA National Centers for Environmental Information (2017). State of the climate: National Climate Report for Annual 2016. Retrieved from www.ncdc.noaa.gov/sotc/national/201612

Nunery, J. S., & Keeton, W. S. (2010). Forest carbon storage in the northeastern United States: Net effects of harvesting frequency, post-harvest retention, and wood products. *Forest Ecology and Management*, *259*(8), 1363–1375. https://doi.org/10.1016/j.foreco.2009.12.029

Oleson, K. W., Lawrence, D. M., Bonan, G. B., Drewniak, B., Huang, M., Koven, C. D., et al. (2013). *Technical description of version 4.5 of the Community Land Model (CLM)*. Boulder, CO: National Center for Atmospheric Research. Retrieved from https://opensky.ucar.edu/islandora/object/technotes:515

Ouimette, A. P., Ollinger, S. V., Richardson, A. D., Hollinger, D. Y., Keenan, T. F., Lepine, L. C., & Vadeboncoeur, M. A. (2018). Carbon fluxes and interannual drivers in a temperate forest ecosystem assessed through comparison of top-down and bottom-up approaches. *Agricultural and Forest Meteorology*, *256-257*, 420–430. https://doi.org/10.1016/j.agrformet.2018.03.017

Papale, D., Reichstein, M., Aubinet, M., Canfora, E., Bernhofer, C., Kutsch, W., et al. (2006). Towards a standardized processing of Net Ecosystem Exchange measured with eddy covariance technique: Algorithms and uncertainty estimation. *Biogeosciences*, *3*(4), 571–583. https://doi.org/10.5194/bg-3-571-2006

Pollack, H. N., & Chapman, D. S. (1977). On the regional variation of heat flow, geotherms, and lithospheric thickness. *Tectonophysics*, *38*(3–4), 279–296. https://doi.org/10.1016/0040-1951(77)90215-3

R Core Team (2016). *R: A language and environment for statistical computing*. Vienna, Austria: R Foundation for Statistical Computing.

Reichstein, M., Falge, E., Baldocchi, D., Papale, D., Aubinet, M., Berbigier, P., et al. (2005). On the separation of net ecosystem exchange into assimilation and ecosystem respiration: Review and improved algorithm. *Global Change Biology*, *11*(9), 1424–1439. https://doi.org/10.1111/j.1365-2486.2005.001002.x

Richardson, A. D., Hollinger, D. Y., Burba, G. G., Davis, K. J., Flanagan, L. B., Katul, G. G., et al. (2006). A multi-site analysis of random error in tower-based measurements of carbon and energy fluxes. *Agricultural and Forest Meteorology*, *136*(1–2), 1–18. https://doi.org/10.1016/j.agrformet.2006.01.007

Sanders-DeMott, R., Ouimette, A. P., Lepine, L. C., Fogarty, S. Z., Burakowski, E. A., Contosta, A. R., & Ollinger, S. V. (2019). Divergent carbon cycle response of forest and grass-dominated northern temperate ecosystems to record winter warming. *Global Change Biology*, *26*, 1519–1531. https://doi.org/10.1111/gcb.14850

Sitch, S., Brovkin, V., von Bloh, W., van Vuuren, D., Eickhout, B., & Ganopolski, A. (2005). Impacts of future land cover changes on atmospheric CO_2 and climate. *Global Biogeochemical Cycles*, *19*, GB2013. https://doi.org/10.1029/2004GB002311

Snyder, W. C., Wan, Z., Zhang, Y., & Feng, Y. Z. (1998). Classification-based emissivity for land surface temperature measurement from space. *International Journal of Remote Sensing*, *19*(14), 2753–2774. https://doi.org/10.1080/014311698214497

Sobrino, J. A., Jiménez-Muñoz, J. C., & Verhoef, W. (2005). Canopy directional emissivity: Comparison between models. *Remote Sensing of Environment*, *99*(3), 304–314. https://doi.org/10.1016/j.rse.2005.09.005

Song, Y., Jain, A. K., & McIsaac, G. F. (2013). Implementation of dynamic crop growth processes into a land surface model: Evaluation of energy, water and carbon fluxes under corn and soybean rotation. *Biogeosciences*, *10*(12), 8039–8066. https://doi.org/10.5194/bg-10-8039-2013

Stange, F., Butterbach-Bahl, K., Papen, H., Zechmeister-Boltenstern, S., Li, C., & Aber, J. (2000). A process-oriented model of N_2O and NO emissions from forest soils: 2. Sensitivity analysis and validation. *Journal of Geophysical Research*, *105*, 4385–4398. https://doi.org/10.1029/1999JD900948

Sun, S. (Ed.). (2005). *Parameterization study of physical and biochemical mechanism in land surface process*. Beijing, China: Meteorology Press.

Tardieu, F., Granier, C., & Muller, B. (1999). Modelling leaf expansion in a fluctuating environment: Are changes in specific leaf area a consequence of changes in expansion rate? *The New Phytologist*, *143*(1), 33–43. https://doi.org/10.1046/j.1469-8137.1999.00433.x

Thorn, A. M., Wake, C. P., Grimm, C. D., Mitchell, C. R., Mineau, M. M., & Ollinger, S. V. (2017). Development of scenarios for land cover, population density, impervious cover, and conservation in New Hampshire, 2010–2100. *Ecology and Society*, *22*(4), 19. https://doi.org/10.5751/ES-09733-220419

Thornton, P. E., Thornton, M. M., Mayer, B. W., Wilhelmi, N., Wei, Y., Devarakonda, R., & Cook, R. B. (2018). *Daymet: Daily surface weather data on a 1-km grid for North America, Version 2*. Oak Ridge, TN: ORNL DAAC.

Urbanski, S., Barford, C., Wofsy, S., Kucharik, C., Pyle, E., Budney, J., et al. (2007). Factors controlling CO_2 exchange on timescales from hourly to decadal at Harvard Forest. *Journal of Geophysical Research*, *112*, G02020. https://doi.org/10.1029/2006JG000293

Williams, C. A., Collatz, G. J., Masek, J., & Goward, S. N. (2012). Carbon consequences of forest disturbance and recovery across the conterminous United States. *Global Biogeochemical Cycles*, *26*, GB1005. https://doi.org/10.1029/2010GB003947

Wilson, K., Goldstein, A., Falge, E., Aubinet, M., Baldocchi, D., Berbigier, P., et al. (2002). Energy balance closure at FLUXNET sites. *Agricultural and Forest Meteorology*, *113*(1-4), 223–243. https://doi.org/10.1016/S0168-1923(02)00109-0

Wilson, M. F., & Henderson-Sellers, A. (1985). A global archive of land cover and soils data for use in general circulation climate models. *Journal of Climatology*, *5*(2), 119–143. https://doi.org/10.1002/joc.3370050202

Wu, X., Vuichard, N., Ciais, P., Viovy, N., de Noblet-Ducoudré, N., Wang, X., et al. (2016). ORCHIDEE-CROP (v0), a new process-based agro-land surface model: Model description and evaluation over Europe. *Geoscientific Model Development*, *9*(2), 857–873. https://doi.org/10.5194/gmd-9-857-2016

Wutzler, T., Reichstein, M., Moffat, A. M., & Migliavacca, M. (2018). REddyProc: Post processing of (half-)hourly eddy-covariance measurements. *R package version*, *1*(1), 3. Retrieved from. https://CRAN.R-project.org/package=REddyProc

Zhang, Y., Li, C., Trettin, C. C., Li, H., & Sun, G. (2002). An integrated model of soil, hydrology, and vegetation for carbon dynamics in wetland ecosystems. *Global Biogeochemical Cycles*, *16*(4), 9-1–9-17. https://doi.org/10.1029/2001GB001838

Zhao, K., & Jackson, R. B. (2014). Biophysical forcings of land-use changes from potential forestry activities in North America. *Ecological Monographs*, *84*(2), 329–353. https://doi.org/10.1890/12-1705.1